OPTIMIZING THE ACCURACY OF TUMOR SEGMENTATION IN PET FOR RADIOTHERAPY PLANNING USING BLIND DECONVOLUTION METHOD

by

Alpaslan KOÇ

B.S., Physics, Boğaziçi University, 2006

M.S., Biomedical Engineering, Boğaziçi University, 2009

Submitted to the Institute of Biomedical Engineering

in partial fulfillment of the requirements

for the degree of

Doctor

of

Philosophy

Boğaziçi University

2019

ACKNOWLEDGMENTS

I came to the end of my student life with this dissertation after a long journey that I saved great memories in the Boğaziçi University. Working on Ph.D. has been not only a wonderful but also an overwhelming process. In any case, I am thankful to many people for turning these long years into an unforgettable experience for me. For this reason, I would like to thank the following contributors for their supports to fulfill my dream.

First, I would like to express my special appreciation to my supervisor, Associate Professor Albert Güveniş, for his initiation and guidance. He always motivated me with his innovative ideas and critical comments. Without his help, this thesis would not end. My special words of thanks should also go to my committee members Professor Cengizhan Öztürk and Professor Ali Yekta Ülgen for their time and scientific advice. In addition, I would like to thank Professor Doctor Mahmut Gümüş and Associate Professor Bora Garipcan for reading and evaluating this thesis.

Finally, I close the circle by thanking those who actually do this thesis. My immediate family has formed the basis for my life that they have given me all the freedom and possibilities that I need. I know everything is not perfect, but my parents have almost made it. For this, I have a lot of respect, thanks pa and ma! Most importantly, my special thanks go to my spouse, Tuba Koç, and my son, Alptuğ Eymen Koç. I am grateful to them for their unconditioned love, sacrifice, support, and patience they have shown me since they were part of my life. This dissertation is dedicated to them.

ACADEMIC ETHICS AND INTEGRITY STATEMENT

I, Alpaslan KOÇ, hereby certify that I am aware of the Academic Ethics and Integrity Policy issued by the Council of Higher Education (YÖK) and I fully acknowledge all the consequences due to its violation by plagiarism or any other way.

Name :

Signature:

Date:

ABSTRACT

OPTIMIZING THE ACCURACY OF TUMOR SEGMENTATION IN PET FOR RADIOTHERAPY PLANNING USING BLIND DECONVOLUTION METHOD

Tumor segmentation accuracy greatly affects the effectiveness of radiotherapy procedures. Maximizing the segmentation accuracy has high medical significance in order to deliver the highest radiation dose to the target volume while protecting the healthy tissues. This dissertation aims to present an optimized method to minimize errors in the automated segmentation of tumors in PET images. Blind deconvolution was implemented in a region of interest encompassing the tumor with an iteration number determined from Contrast-to-Noise Ratios. The images were resampled. Several automatic segmentation algorithms were tested on three datasets: phantom, simulated geometric lesions inserted in real images, and simulated clinical images with real heterogeneous tumors for which ground truth was known. The volumes of the tumors were 0.49-26.34 cc, 0.64-1.52 cc, and 40.38-203.84 cc respectively for the three datasets. The widely available software tools MATLAB, MIPAV, and ITK-SNAP were used. With the use of the active contour with classification technique, the mean errors were reduced from 95.85% to 3.37%, from 815.63% to 17.45%, and from 32.61% to 6.80% for all the lesions of the phantom dataset, the simulated dataset, and the large lesions of the clinical PET dataset respectively. The computational time was reduced by a factor of more than 10 by the use of region-of-interest-based deconvolution. Contrast-to-Noise Ratio and Region-of-Interest based deconvolution have the potential to improve delineation accuracy for different sizes of homogeneous and heterogeneous tumors. Improvement is very important for smaller tumors. The algorithm may provide reduced computational time with respect to full deconvolution and can be implemented using widely available software tools.

Keywords: PET, medical image segmentation, image restoration, blind deconvolution, radiotherapy planning.

ÖZET

RADYOTERAPİ PLANLAMASI İÇİN PET TÜMÖR SEGMENTASYON DOĞRULUĞUNUN KÖR DEKONVOLÜSYON METODU İLE OPTİMİZE EDİLMESİ

Tümör segmentasyon doğruluğu, radyoterapinin etkinliğini büyük ölçüde etkiler. Segmentasyon doğruluğunun artması, sağlıklı dokuları korurken hedef hacime en yüksek radyasyon dozunu sağlamak için önemlidir. Bu tez, PET tümör segmentasyon hatalarını minimize edebilecek bir yöntem sunmayı amaçlamaktadır. Bu nedenle, tümör bölgelerinde, Kontrast-Gürültü oranları ile parametreleri optimize edilen kör dekonvolüsyon metodu kullanılmıştır. 3-boyutlu görüntüler üzerinde dekonvolüsyon öncesinde yeniden örnekleme yapılmıştır. Gerçek tümör hacimleri bilinen, üç veri seti üzerinde (fantom, klinik PET görüntüleri içerisine yerleştirilmiş küçük tümörler ve simüle edilmiş klinik PET görüntüleri), çeşitli otomatik bölütleme algoritmaları test edilmiştir. Kullanılan tümörlerin hacimleri, üç veri seti için sırasıyla 0.49-26.34 cc, 0.64-1.52 cc ve 40.38-203.84 cc arasında değişmektedir. Görüntü işlemede yaygın olarak kullanılan MATLAB, MIPAV ve ITK-SNAP yazılımları kullanılmıştır. Ölçülen ortalama hacim hataları, sınıflandırma tekniğine sahip aktif kontur segmentasyon metodu ile fantomun tüm lezyonları için ortalama %95.85'ten %3.37'ye, klinik PET görüntüleri içerisine yerleştirilmiş simüle geometrik lezyonlar için %815.67'den %17.45'e ve büyük lezyonlara sahip klinik PET görüntüleri için %32.61'den %6.80'e düşmüştür. Tümör temelli dekonvolüsyon metodunun kullanımıyla hesaplama süresi ortalama 10 kattan fazla azalmıştır. Kontrast-Gürültü oranı ve tümör dayalı dekonvolüsyon, farklı boyutlardaki homojen ve heterojen tümörler için segmentasyon doğruluğunu geliştirme potansiyeline sahiptir. İyileştirme, küçük tümörler için çok önemlidir. Algoritma, tüm görüntünün dekonvolüsyonuna göre düşük hesaplama süresi sağlamakta ve yaygın olarak kullanılan yazılım araçları ile uygulanabilmektedir.

Anahtar Sözcükler: PET, tıbbi görüntü bölütleme, görüntü iyileştirme, kör dekonvolüsyon, radyoterapi planlaması.

TABLE OF CONTENTS

ACKNOWLEDGMENTS iii
ACADEMIC ETHICS AND INTEGRITY STATEMENT iv
ABSTRACT v
ÖZET vi
LIST OF FIGURES ix
LIST OF TABLES xii
LIST OF SYMBOLS xiv
LIST OF ABBREVIATIONS xvi
1. INTRODUCTION 1
1.1 Motivation 1
1.2 Aims 2
1.3 Contributions 2
1.4 Outline of the Thesis 3
2. BACKGROUND AND RELATED WORKS 5
2.1 PET Image Segmentation Methods 5
2.1.1 Thresholding method 6
2.1.2 The stochastic and learning-based methods 7
2.1.3 Region-based method 8
2.1.4 The boundary based method 9
2.1.5 Segmentation Evaluation Metrics 11
2.2 Partial Volume Effect 16
2.3 Image Restoration with Blind Deconvolution 20
3. MATERIAL AND METHODS 23
3.1 Data 23
3.1.1 Dataset 1: The Phantom Data 23
3.1.2 Dataset 2: The Realistic Simulated Whole Body ^{18}F-FDG PET Oncology Images 24
3.1.3 Dataset 3: Clinically Relevant Large Tumors with Irregular Shapes and Non-uniform Activity Distributions 25

3.2 The Local Extraction Method: Cropping 26
3.3 Resampling 27
3.4 Blind Deconvolution 28
3.4.1 Determination of the Initial PSF Size and the Iteration Value . 29
3.5 Quantitative Evaluation Criterion for the Best PSF Size and Iteration Value 30
3.6 Segmentation Methods 35
3.6.1 Adaptive Thresholding Method 35
3.6.2 Maximum Entropy Thresholding 36
3.6.3 Region Growing Method 37
3.6.4 Active Contour with Classification Method 39
3.6.5 Fuzzy C-Means Segmentation Method 40
3.7 Error Evaluation Metrics 42
3.8 Structure of the Study 43
3.9 Statistical Analysis 43
4. RESULTS 45
4.1 Results of the Phantom Data 45
4.2 Results of the Realistic Simulated Whole Body ^{18}F-FDG PET Oncology Images 51
4.3 Results of the The Clinically Relevant Large Tumors 54
5. DISCUSSION 59
5.1 Main Findings 59
5.2 Comparison with Literature 63
5.3 Limitations and Future Work 66
6. CONCLUSION 67
6.1 List of publications produced from the thesis 67
APPENDIX A. BLIND DECONVOLUTION ALGORITHM 69
REFERENCES 71

LIST OF FIGURES

Figure 2.1 The intensity profile of the real object (ideal case) (a), and acquired image (real case) (b). Note that in real case, the intensity profile is seen as larger and weaker than it actually is due to the PVE (c). 16

Figure 2.2 An ideal object (a), and its acquired image (b). Note that signal intensity is reduced due to the limited sampling grid size in (b) (tissue fraction effect). 17

Figure 2.3 Schematic illustration of a general image restoration process. 21

Figure 3.1 The central slices of the PET (a), CT (b), and manually segmented lesions (c). Note that volume measurement error of each segmentation technique is calculated before and after restoration with respect to reference volumes obtained from active epoxy volume values and manually segmented CT volumes. 24

Figure 3.2 The coronal slices of 3-D whole-body ^{18}F-FDG PET images with the lesion size of 14 mm at SBR of 10:1 (a), the lesion size of 14 mm at SBR of 4:1 (b), the lesion size of 10.5 mm at SBR of 10:1 (c), and the lesion size of 10.5 mm at SBR of 4:1 (obtained from the reference [48]). 25

Figure 3.3 The visual illustration of the central slices in tumors and ground truth masks obtained from the Dataset 3. 26

Figure 3.4 General iterative blind deconvolution method based on the Lucy-Richardson Algorithm. 28

Figure 3.5 The central slice of the phantom lesion with size of 17 mm at SBR of 4:1 and its 3D surface plot before deconvolution (a), and after deconvolution (b). 30

Figure 3.6 The lesion VOI was selected on the central slice of the phantom lesion with size of 17 mm at SBR of 4:1 (a), and a 3-D lesion VOI and a 3-D background VOI were formed to evaluate convergence rate of the deconvolution processes (b). 31

Figure 3.7 Seed point selection and 3-D region growing segmentation of the spherical phantom lesion with size of 17 mm at SBR of 4:1 for original image (a), and restored image (b). 38

Figure 3.8 Active contour segmentation with classification method of the spherical phantom lesion with size of 17 mm at SBR of 4:1 for the restored image. 40

Figure 3.9 Overlap measurement method for segmented and ground truth voxels. 43

Figure 3.10 The methodology of our study. 44

Figure 4.1 Mean absolute volume errors of the segmentation methods for original and restored phantom images (Dataset 1). 47

Figure 4.2 Comparisons of measured lesion volumes with ground truth volumes with respect to five segmentation methods (Dataset 1). Adaptive Thresholding in (a), Maximum Entropy Thresholding in (b), Region Growing in (c), Active Contour with Classification in (d), and Fuzzy C-Means Segmentation in (e). The dotted line shows where the measured volume and true volume are equal. These data belong to six spherical lesions with volumes ranging from 0.49 to 26.34 cc. Note that x and y-axes are plotted on a logarithmic scale with base 2. 48

Figure 4.3 Intensity profiles of the original and restored phantom lesions at SBR of 4:1 (Dataset 1). Note that for each lesion, original and recovered images are displayed on the left side and on the right side, respectively. 50

Figure 4.4 Measured lesion volumes using various PET image segmentation methods with and without blind deconvolution for Dataset 2. 53

Figure 4.5 Intensity profiles of the original and restored simulated PET Oncology images (Dataset 2). 54

Figure 4.6 Intensity profiles of the original and restored clinically relevant patient images (Dataset 3). 58

Figure 5.1 The chart that summarizes the performance of the segmentation methods on phantom lesions in terms of VE%. Note that AT is the Adaptive Thresholding, MET is the Maximum Entropy Thresholding, RG is the Region Growing, ACWC is the Active Contour with Classification, and FCM is the Fuzzy C-Means segmentation methods. 61

Figure 5.2 CNR values for all lesions before and after restoration (a), CNR values with respect to iterations are shown in (b) for the dataset 1, in (c) for the dataset 2, and in (d) for the Dataset 3. 64

LIST OF TABLES

Table 2.1	Literature studies about PET image segmentation methods.	12
Table 3.1	Ground truth sphere volumes of the phantom data.	24
Table 3.2	Ground truth volumes of the Dataset 3.	26
Table 3.3	Physical properties of the locally extracted regions.	27
Table 3.4	CNR values of the original and restored images at fix iteration value of 1.	33
Table 3.5	Best parameter and CNR values for various lesions.	33
Table 3.6	CNR values of the original and restored images at various iteration values for given best PSF kernels.	34
Table 3.7	Threshold intensity values for adaptive segmentation algorithm.	36
Table 3.8	Measured seed point locations in pixels and intensities for original and restored images.	38
Table 4.1	Segmentation results and absolute percentage errors of the Dataset 1 with respect to various segmentation techniques for original and restored cases.	46
Table 4.2	Overlap measurements (JI) in relation to real volumes of the spheres obtained from Dataset 1.	49
Table 4.3	Segmentation results and absolute percentage errors of the Dataset 2 with respect to various segmentation techniques for original and restored cases.	52
Table 4.4	Segmentation results and absolute percentage errors of the Dataset 3 with respect to various segmentation techniques for original and restored cases.	55
Table 4.5	Overlap measurements (JI) in relation to real volumes of the spheres obtained from Dataset 3.	56
Table 5.1	The comparison of the execution times of the local blind deconvolution and the whole image blind deconvolution (obtained from the reference [48]).	62
Table 5.2	Comparison of the state-of-the-art studies with our method.	66

Table A.1 Edgetaper kernel sizes used to reduce ringing artifacts for various lesion sizes. 69

LIST OF SYMBOLS

$V_{measured}$	Measured lesion volume
V_{true}	Real lesion volume
V_{seg}	Number of voxels inside segmented regions
V_{true}	Number of voxels inside ground truth regions
$g(x, y, z)$	Blurred 3-D image
$f(x, y, z)$	Real 3-D object
$H(x, y, z)$	3-D PSF of the system
$n(x, y, z)$	Additive poisson noise
J	The estimation of the real image ($f(x, y, z)$)
PSF	The final estimation of the blurring function $H(x, y, z)$
I	The observed image $g(x, y, z)$
$INITPSF$	The initial estimation of the blurring function
$NUMIT$	Number of iteration value
H_{i+1}^k	The new estimated PSF at kth iteration
H_i^k	The estimated PSF from the previous R-L iteration i
f_{i+1}^k	The new restored object at kth iteration
(f^{k-1})	The restored object from the k-1 blind iteration
f_i^k	The restored object from the previous R-L iteration i
(H^k)	Estimated PSF obtained from the output of the first cycle
L_{mean}	The mean activity inside the lesion
B_{mean}	The mean activity inside the background
STD_B	SD of the activity inside the background VOI
g_i	Gray levels of the voxels
αg_I	The outward direction force
κ	The mean curvature of the contour
g_I	The speed function
$\vec{N}$	The unit vector normal to the contour
$\gamma(\nabla g_I \vec{N})$	The inward direction force

α, β, and γ	Weights of the function
μ_{ik}^{q}	Membership value at pixel location k for class i
q	The weighting factor that controls the membership value
x_k	The observed intensity at location k
v_i	The center of the cluster i
c	The number of the clusters
$\|x_k - v_i\|^2$	Distance between the object and the centroid

LIST OF ABBREVIATIONS

RTP	Radiation Treatment Planning
CT	Computed Tomography
MRI	Magnetic Resonance Imaging
^{18}F-FDG PET	18F-Fluorodeoxyglucose Positron Emission Tomography
PVE	Partial Volume Effect
PSF	Point Spread Function
PVC	Partial Volume Correction
SBR	Signal to Background Ratio
SUV	Standardized Uptake Value
GMM	Gaussian Mixture Model
EM	Expectation Maximization
FLAB	Fuzzy Locally Adaptive Bayesian
AT	Adaptive Thresholding
FCM	Fuzzy C-Means
KNN	K-Nearest Neighbor
ANN	Artificial Neural Network
SVM	Support Vector Machine
RG	Region Growing
GRAD$^{\mathrm{WT}}$	Gradient-based Watershed segmentation method
ACWE	Active Contour Without Edges
ACWC	Active Contour With Classification
DSC	Dice Similarity Coefficient
CE%	Classification Error Percentage
JI	Jaccard Index
RC	Recovery Coefficient
GTM	Geometric Transfer Matrix
LR	Lucy-Richardson Deconvolution
FWHM	Full Width at Half Maximum

CRC	Contrast Recovery Coefficient
CoV	Coefficient of Variation
RMSE	Root Mean Square Error
MLEM	Maximum Likelihood Expectation Maximization
FOV	Field of View
MATV	Metabolically Active Tumor Volume
TLG	Total Lesion Glycolysis
AC	Active Contour
GVF	Gradient Vector Field
CNR	Contrast to Noise Ratio
NEMA	National Electrical Manufacturers Association
VOI	Volume of Interest
MET	Maximum Entropy Thresholding
ROI	Region of Interest

1. INTRODUCTION

Radiation therapy is one of the most important treatment methods. It uses several types of ionizing radiation such as x-rays, gamma rays or electron beams to kill cancer cells or to prevent the spread of them. Ultimately, its aim is to remove the cancer tissues by damaging the DNA of these cells doing the least harm to the healthy tissues [1, 2].

Radiation Treatment Planning (RTP) consists of many levels which are patient data acquisition and simulation, volume delineation, treatment time, optimization, plan evaluation and quality assurance. This treatment planning begins with procedures for identifying and localizing volumes of tumor cells. Therefore, volume segmentation process plays a crucial role among these steps for RTP and is generally based on getting information from imaging modalities such as Computed Tomography (CT) and Magnetic Resonance Imaging (MRI).

However, current trends in RTP have led to the increased use of [^{18}F]-2-Deoxy-2-fluoro-d-glucose Positron Emission Tomography (^{18}F-FDG PET) images to identify metabolic tumor volume [3]. It is of utmost importance to be able to determine the volume of a tumor in an accurate way in order to deliver the highest radiation dose to the target volume while protecting the healthy tissues so that the curative outcome of the treatment planning process can be improved and the chance of survival of the patient can be increased [4].

1.1 Motivation

Volume delineation is generally carried out by manually drawn contours around lesions. In addition, several automatic and semi-automatic tumor delineation techniques have been proposed and used in clinical settings. However these techniques have

varying accuracy and their performance is affected by intrinsic and/or extrinsic factors, i.e., image acquisition and reconstruction, artifacts, noise, patient-related factors, tracer uptake, and imaging system itself.

If the tumor size is less than 2 or 3 times the spatial resolution of the PET imaging system ($\sim$5 mm), the tumor is seen larger than its real size within the reconstructed image. This distortion is known as the Partial Volume Effect (PVE) which stems from the result of the convolution of the real object and the Point Spread Function (PSF) of the system [5]. PVE causes errors in tumor radiopharmaceutical uptake measurements and segmentation processes. Therefore, maximizing segmentation accuracy is still an unresolved problem despite its high medical significance.

1.2 Aims

This dissertation aims to study the impact of the PVE on the accuracy of segmentation algorithms and to optimize the accuracy with respect to best parameters of the post-reconstruction based Partial Volume Correction (PVC) technique (the blind deconvolution method) under varying tumor sizes and Signal to Background Ratio (SBR) conditions. Therefore, the primary motivation is fundamentally to help guide medical professionals in making better segmentation that will ultimately benefit their patients.

1.3 Contributions

It is very important to enhance images for varying tumor shapes, sizes, and activity distributions in order to obtain accurate and precise volume segmentation. Therefore, we improved the accuracy of the various PET segmentation algorithms for volume quantification in PET images combining two methods (the local blind deconvolution and the resampling method). Very few studies have been conducted to investigate the

effect of blind deconvolution on PET segmentation methods based on the evaluation of best deconvolution parameters. The issues that will answer the following questions will be identified as the original/innovative aspects of our study.

1. How can PET tumor segmentation accuracy be improved by using a post-reconstruction-based restoration method with a lower computational cost without knowing the real object itself and the distortion function of the system (PSF)?
2. Which segmentation methods will yield minimum segmentation errors depending on the restoration and lesion characteristics?
3. Is there a relationship between restoration parameters and Contrast-to-Noise Ratio (CNR) in terms of lesion characteristics?
4. What set of deconvolution parameters will ensure accurate and robust delineation for the best segmentation method?
5. What is expected from a delineation methodology for PET and/or PET/CT?

1.4 Outline of the Thesis

This dissertation is composed of six chapters, each of them dealing with different aspects of the study. The motivation and aim of the study were explained in Chapter 1. Chapter 2 is subdivided into three parts and presents the theoretical background and most recent developments. Part 1 describes PET segmentation methods and explains the relevant literature. Part 2 deals with the PVE and presents recent studies on PVC methods. In Part 3, the blind deconvolution technique and its implementation were being investigated. Materials and methods of the study were given in Chapter 3. Implementation strategy of the blind deconvolution method, the segmentation techniques used, and their evaluation criteria were explained in detail in subsections of Chapter 3. Chapter 4 concentrates on the results obtained from three datasets. Reviews of the findings, the comparison of results with recent literature studies, and limitations of the

study were given in Chapter 5. Finally, the dissertation is concluded in Chapter 6 by emphasizing the significance of the findings and future works.

2. BACKGROUND AND RELATED WORKS

There is a large volume of published studies describing the role of the PVE in quantification of radioactivity in nuclear medicine images. In addition, several correction algorithms have been developed to prevent the PVE, to enhance image quality, and to obtain accurate and precise measurements of tracer uptake in tumors. The first section of this chapter will present PET image segmentation methods and examine relevant literature studies. The second section of this chapter will focus on the PVE. Finally, the last section of this chapter will explain and examine the blind deconvolution method and recent developments.

2.1 PET Image Segmentation Methods

The tools for RTP have been amended, but the basic volume delineation process remains mostly the same [1]. Delineation of lesion volume is generally carried out by physicians using image segmentation techniques or manually drawn contours around lesions. Therefore, the latter substantially depends on the experience of the physician and causes intra-observer and inter-observer variability. Simple manual thresholding, which is normally used to segment a PET tumor, is not appropriate due to the lack of standardized value. Such automated tumor delineation methods as thresholding, region growing, classifiers, clustering, edge detection, Markov random field models, deformable models, and many other methods have been reviewed in [6, 7].

In their literature survey, Foster et al. have classified the PET image segmentation methods as manual, thresholding-based, stochastic- and learning-based, region-based, boundary-based, and joint segmentation methods [6]. In the following, current literature is given to describe recently developed PET tumor segmentation algorithms. In each subsection of this part, a brief overview of segmentation techniques and literature studies will be presented. Also, these studies will be examined further in Table

2.1 in terms of segmentation results.

2.1.1 Thresholding method

Thresholding method is the most widely used segmentation method thanks to its simplicity and efficiency in the RTP. A Threshold value (T) is determined and compared with image pixel or voxel intensity value ($I(x)$) to classify two regions as lesion and background within an image.

$$Lesion = T[I(x)] = \begin{cases} 1, \ I(x) \geq T \\ 0, \ I(x) < T \end{cases} \tag{2.1}$$

The intrinsic and extrinsic factors may cause fuzziness in the lesions' boundaries. Therefore, identifying the optimal threshold value is critical for better delineation.

The literature cites three types of threshold selection methods (fixed, adaptive, and iterative thresholding method). Despite the widely used thresholding values (the Standardized Uptake Value (SUV) of 2.5 and the 40 - 43% of SUV_{max}), there is no consensus among researchers [6]. Threshold values may not be adequate, particularly for small lesions, if they can not be adjusted for foreground and background regions. Therefore, several groups of researchers adapted the optimum threshold value drawing upon various metrics such as the estimated mean foreground and background intensity (Nestle's method), SBR (Daisne's method), SUV (Schaefer's method), and lesion physical parameters [8–15]. It appears from Table 2.1, most researchers drew on at least one thresholding technique to test their new segmentation methods developed [4, 16–26]. These studies have shown that although the thresholding method is simple and effective in terms of applicability and time, its performance is not superior compared with new segmentation methods.

2.1.2 The stochastic and learning-based methods

The stochastic models use statistical differences in intensity distribution between tumor uptake and surrounding normal tissues. The Gaussian Mixture Model (GMM), the Expectation Maximization (EM) algorithm, and the Hidden Markov Models are the most widely used methods for image segmentation approach. Hatt et al. developed a new segmentation algorithm, called Fuzzy Locally Adaptive Bayesian (FLAB), based on the Gaussian mixtures of the object and Bayesian statistics [17]. They compared the FLAB technique with other segmentation methods and found that their method showed better performance on segmentation of phantom and clinical images.

In another study, they developed a three classes FLAB method for segmentation of heterogeneous and irregular lesion volumes [18]. They reported that the 3-FLAB method is better than the other methods (the Adaptive Thresholding (AT) methods, the Fuzzy C-Means (FCM), and the FLAB). However, none of the segmentation methods used have resulted in a reasonable estimate for volumes of lesions smaller than 20 mm in diameter.

In a further study, they evaluated the robustness and repeatability of the FLAB method and compared with the FCM and various thresholding methods [19]. This method had considerably better performance than the other methods even in nonuniform and small lesions (Mean CE%±SD%: 8.7%±4.5%). Another phantom study compared the FLAB segmentation method with the various thresholding algorithms (fixed thresholding (T40% and T50%), adaptive thresholding (AT40 and AT50), and contrast oriented (CT) methods) [25]. Firouzian et al. recommended that CT and AT40/AT50 are the best choices for all lesion sizes compared with the FLAB method.

Learning methods are techniques developed to estimate dependency on data in pattern recognition. Based on a set of extracted features from images, the learning task discriminates against tracer uptakes between the lesion and surrounding normal tissue voxels. Supervised (classification) and unsupervised (clustering) learning methods are used in this process. Supervised learning is used to estimate unknown mapping from

known labeled samples, i.e., it needs training data. In unsupervised learning, only input samples are given to the learning system, i.e., this method does not require training data.

Commonly used classifiers include K-Nearest Neighbor (KNN), Artificial Neural Network (ANN), and Support Vector Machine (SVM). These methods have seen limited applications in PET. On the other hand, clustering methods have shown more promise for segmentation of PET tumors. Among the stochastic and learning-based segmentation methods, the spectral clustering, the FCM, the K-Means algorithm, and the EM algorithm are the frequently used clustering methods.

As seen in Table 2.1, segmentation of phantom, simulated and clinical lesions have been carried out using the FCM method and other segmentation techniques [17–20, 23]. Dewalle-Vignion et al. developed a new segmentation method (Possibility Theory based method) and compared it with the FCM and other methods [20]. They reported that their method resulted in better segmentation performance compared to other methods (the FCM, fixed thresholding, and adaptive thresholding) for phantom and simulated lesions. The FCM yielded higher errors compared to others. In the studies of Hatt et al. [17–19], they used the FCM method and thresholding methods to compare with their new segmentation method (the FLAB method). Their results showed that the FCM method has higher accuracy than thresholding methods, but lower than the FLAB method. Similarly, in the study of Zaidi et al. [23], they found that the FCM method provided better results than the thresholding method (Schaefer's method).

2.1.3 Region-based method

The region-based method consists of the Region Growing (RG), the Graph-Cut, and the Random Walk methods [6]. In the RG, the initial seed location, the mean and the standard deviation of voxel intensities in lesion regions are the main concern for accurate segmentation of lesions. The algorithm starts at an initial seed point

and determines the lesion boundary by connecting this starting point with the nearby voxels depending on similarities of lesion voxels.

In 2008, Li et al. published a paper in which they used region growing algorithm with active contour model to accurately delineate a lesion in PET image [27]. They reported that the combined method showed better performance than iterative threshold method in terms of volume estimation accuracy for the volume of tumors less than 6 mL. Despite prior results, the RG method may not be sufficient for segmentation of the lesions with heterogeneous uptake distributions and higher level of noise.

2.1.4 The boundary based method

The boundary based method is classified into the gradient based method and the level set/active contour method. The first method uses information provided by gradient differences between the lesion and the background for the segmentation task [7]. Therefore, boundaries or edges of the object should provide adequate discrimination from the background regions. In general, edges of small tumors are more blurry than larger ones due to the PVE, noise and reconstruction artifacts. Thus, iterative deconvolution algorithms, and simple edge or ridge detectors such as Sobel, Prewitt, and Roberts filters are implemented before clustering analysis.

The Gradient-based Watershed segmentation method (GRAD^{WT}) was first applied by Geets et al. on PET images [16]. They compared the segmentation performance of the GRAD^{WT} method with the SBR dependent threshold method (Daisne's method) for with and without denoising and deblurring processes. They observed that the GRAD^{WT} method performed better segmentation results than the threshold method. The volume error percentage value (VE%) ranged from 20% to 10% for the smallest to the largest sphere (their volumes range from 2.1 mL to 92.9 mL). In another study, Cheebsumon et al. compared the GRAD^{WT} method with the fixed, the adaptive, and the iterative thresholding methods using phantom and simulated data [4]. Unlike Geets et al, they reported that the contrast oriented thresholding method (the Schaefer's

method) showed superior performance compared to others in terms of segmentation accuracy for lesions bigger than 20 mm in diameter.

The active contour model is a technique that evolves a contour using internal and external energy functions until it reaches the boundary of the object. Internal energy is a smoothing force derived from an object's geometry. External energy is an image force that moves the contour inward and outward directions to fit on the objects where the edges exist. Chan et al. redesigned the external energy function using regional information of the image for the Active Contour Without Edges (ACWE) method [28]. Khamwan et al. integrated the shifted-optimal thresholding into the ACWE method and compared its segmentation performance with manual, thresholding, and the ACWE methods [21]. The results are presented in Table 2.1. Their proposed automated method improved the segmentation accuracy and precision of the PET tumors compared to others. In another study, Abdoli et al. modified the ACWE method using anisotropic diffusion filtering and contourlet transform on PET images [29]. Moreover, they compared this method with the thresholding, the FCM, and the FCM-SW methods. In contrast to Zaidi et al. [23], they concluded that their proposed method has superior performance than other three methods in tumor segmentation.

The studies presented thus far indicate that the active contour methods used are highly operator dependent, therefore Zhuang et al. developed a new automated active contour segmentation method using histogram FCM clustering and textural information. This method forces the contour without user defined parameters for detection of the object's boundaries [26]. As can be seen from Table 2.1, their proposed method provided better results compared to the thresholding and the counterlet active contour methods in terms of the DSC (0.71) and the CE% (54%) except the VE% (11%).

2.1.5 Segmentation Evaluation Metrics

The extent to which a delineation method is suitable, i.e., whether it is applicable or not for specified cases, is measured through validation studies depending on the set of images included and quality criteria. Therefore, validation is an important step in this process and is carried out by simulations, phantoms, or patient data. Various figures of merit can evaluate the efficiency of delineation methods. The simplest measurement is comparing the volume of a delineated lesion with its true value, and it is measured by Volume Error Percentage (VE%) as shown in Eq. 2.2:

$$VE\% = \frac{|V_{measured} - V_{true}|}{V_{true}} \times 100 \tag{2.2}$$

where $V_{measured}$ is the measured lesion volume and V_{true} is the true lesion volume [16].

However, volume overlap measurement should be done to prevent complications in case of equal volumes. The Jaccard Index (JI) [24], the Classification Error (CE) [17], and the Dice's Similarity Coefficient (DSC) [23] are commonly used evaluation metrics related to the amount of correctly and incorrectly segmented voxels for interested objects. Eq. 2.3 and Eq. 2.4 show the calculation of the JI value and the DSC respectively.

$$JI = \frac{(V_{seg} \cap V_{true})}{(V_{seg} \cup V_{true})} \tag{2.3}$$

$$DSC = \frac{2(V_{seg} \cap V_{true})}{(V_{seg}) + (V_{true})} \tag{2.4}$$

$(V_{seg} \cap V_{true})$ is the number of voxels inside both segmented and ground truth regions, (V_{seg}) is the number of voxels inside the segmented region and (V_{true}) is the number of voxels inside the ground truth region. The JI and the DSC have a value between 0 (no overlapping voxels between two regions) and 1 (two areas are completely overlapped).

Table 2.1 Literature studies about PET image segmentation methods.

Literature Studies	Data	Segmentation Methods	Evaluation Metrics	Notes
Cheebsumon et al. (2011) [4]	**1)Nema IQ Phantom Data** with 6 spheres (Size: 10-37 mm, SBR: 5 and 9). **2)Simulation Data:** Computer generated image of thorax with 5 lesions (Size: 10-50 mm, SBR: 4, 8, and 12), Lesions are segmented before and after smoothing (Gaussian Kernel: 5, and 7 mm) and denoising (edge preserving bilateral filter) processes.	**1)Fixed thresholding** (T41%, T50%, T70%) **2)Adaptive thresholding** (AT41, AT50, AT70) **3)Contrast oriented method** ($VOI^{Schaefer}$) **4)Background-subtracted relative threshold level method** (VOI^{RTL}) **5)Gradient based watershed method** ($Grad^{WT}$) **6)$SUV^{2.5}$**	**VE%**	1) Tumor delineation accuracy improved with denoising and smoothing. 2) The $VOI^{Schaefer}$ method is the best for the spheres larger than 20 mm in size.
Dewalle-Vignion et al. (2011) [20]	**1)Nema IQ Phantom Data** with 6 spheres (Size: 10-37 mm, SBR: 4.3 and 8.9) / Matrix size: 128x128x75 / Voxel size: 5.47x5.47x3.27 mm^3 / Rec: OSEM, 2 it, 21 subsets / 6 mm Gaussian smoothing. **2)Simulation Data:** Lesions (Volume: 0.7-56.45 mL) with uniform tracer distributions are simulated by GATE simulation platform. / Matrix size: 144x144x87 / Rec: OSEM, 5 it, 10 subsets. **3)Clinical Data:** Patient's anatomopathological data (Vol: 6.58-40.82 mL)	**1)Possibility Theory based segmentation** **2)T42%** **3)Contrast oriented method** (Nestle's method) **4)Daisne's method** **5)FCM**	**1)VE%** **2)DSI** **3)CE**	**1)Nema IQ Phantom:** For all spheres included except the sphere size of 10 mm, VE%s of the possibility theory based segmentation are 19.75%±9.94% and 15.45%± 6.96% at SBR of 4.3 and 8.9, respectively. **2) Simulation Data:** 24.08% ± 30.38% for SUV=2.5 15.70% ± 18.71% for SUV=4.5 11.85% ± 11.48% for SUV=6 (results from the possibility theory based segmentation) **3) Clinical Data:** The FCM method gives unsatisfactory results compared with others. The T42% performs better results for higher SUV value compared with others (due to less noise). The Nestle's, the Daisne's, and the Possibility Theory-based segmentation methods yield about 23% segmentation errors.
Firouzian et al. (2014) [25]	**1)Nema IQ Phantom Data** with 6 spheres (Size: 10-37 mm, SBR: 4 and 8) / Matrix sizes: 200x200 and 400x400 / Voxel sizes: 4.073x4.073x2.027 mm^3 and 2.036x2.036x2.027 mm^3 / Rec: 4 types of rec. alg. / Counts: 3.10^7 and 6.10^7 **2)Synthetic Phantoms:** The first phantom consists of 7 spheres (Size: 7-37 mm). The second phantom includes spheres with necrotic core (Size: 7-37 mm). The third phantom contains 6 lesions of irregular shapes from real patient data.	**1)Fixed thresholding** (T40%, T50%) **2)Adaptive thresholding** (AT40, AT50) **3)Contrast oriented method** (CT) **4)FLAB**	**1)VE%** **2)SI**	**1)Nema IQ Phantom:** For all spheres, CT is the best one. The VE% is 5.56% ± 24.34%. **2) For small spheres (<17 mm):** CT, AT40, and AT50 have given sensible results. **3) For images with irregular tumor shapes:** AT40 is the best after using Gaussian filter: SI=0.61, VE%=14.83% ± 49.39%

Continued on next page

Table 2.1 – *Continued from previous page*

Literature Studies	Data	Segmentation Methods	Evaluation Metrics	Notes
Geets et al. (2007) [16]	**1)Computer generated phantom images:** Cylindrical phantom with 5 spheres (Sizes: 20-46 mm, Vol: 4.19-50.97 mL, SBR: 6) / Matrix size: 128x128x47 / Denoising and deblurring are implemented using the edge preserving filter and the constrained iterative deconvolution. **2)Lucite phantom images:** Cylindrical phantom with 6 spheres (Vol: 2.1-92.9 mL, SBR: 1.5-15) / Matrix size: 128x128x47 / Rec: 3D OSEM **3)Patient images:** 7 patients with squamous cell carcinoma / Ground truth: Delineated by pathologists.	**1)The Gradient-based watershed** ($Grad^{WT}$) **2)Thresholding method** (The Daisne's method: SBR dependent threshold method)	1)VE% 2)Regression curves. 3)Mean volume.	**1)On the first dataset**, the VE% values ranged from 13.98% to 3.16% without deblurring, and -3.17% to 1.81% with deblurring for smallest to largest sphere. **2)On the second dataset**, the VE% ranged from 20% to 10% for smallest to largest sphere. **3)On the third dataset**, the gradient-based method was the best compared with the thresholding method. (R^2 = 0.88, and 0.67 for the gradient-based method and the thresholding method, respectively.)
Hatt et al. (2009) [17]	**1)Nema IQ Phantom:** The data includes 6 spheres (Size: 10-37 mm, SBR: 4 and 8) / Voxel sizes: 2x2x2 mm^3 and 4x4x4 mm^3 / Rec: 3D RAMLA / Philips Gemini PET Scanner / Spatial Res: 4.9 FWHM at the center of FOV / Ground Truth: CT image / 1,2, and 5 min. list-mode time frames. **2)Clinically Realistic Data:** GATE simulation platform simulates 3 lesions which have non-uniform activity distributions and shapes. Lesions are located in the lung. / Voxel sizes: 2x2x2 mm^3. Lesion 1: Size: 41 mm, SBR: 6:1 Lesion 2: Size: 29 mm, SBR: 5:1 Lesion 3: Size: 15 mm, SBR < 2:1	**1)Fixed thresholding** (T42%) **2)FCM** **3)FHMC** **4)FLAB**	**1)VE%** **2)CE**	**1)Results of phantom lesions with the 4x4x4 mm^3 voxel size at the SBR of 4:1** **The 10-mm lesion:** T42%, FCM, FHMC, and FLAB: >100% error **The 13-mm lesion:** T42%, FCM, and FHMC: >100% / FLAB: 0-10% (5min), 10-20% (2min) **The 17-mm lesion:** T42%: >100% / FCM: ≈30% / FHMC: 20-30% / FLAB: <10% **The 22-mm lesion:** T42%: ≈30% / FCM, FHMC, and FLAB: <10% **The 37-mm lesion:** T42%: 10-20% / FCM, FHMC, and FLAB: <10% **2) Clinical Image Results:** **Lesion 1:** T42%: 40-50% / FCM: 30-40% / FHMC, and FLAB: <10% **Lesion 2:** T42%, FCM, FHMC, and FLAB: <10% **Lesion 3:** T42%: >50% / FCM: 20-30% / FHMC: 10-20% / FLAB: <10%
Hatt et al. (2010) [18]	**1)Simulated Tumors:** 20 realistic tumors which have irregular shapes with uniform and nonuniform uptake distributions are simulated by GATE for PET/CT scanners. Rec.: OPL-EM with 7 it. and 1 subsets / Vox. size: 4x4x4 mm^3 and 2x2x5 mm^3 / Ground truth: Manual delineation by nuclear medicine experts. **2)Clinical Data:** 18 lung tumors of patients. / Size: 15-90 mm / Rec: OSEM with 4 it. and 8 subsets / Vox. size: 5.31x5.31x5.31 mm^3 / Ground truth: Histologic examination.	**1)Adaptive thresholding** (AT, Nestle's method) **2)FCM** **3)FLAB** **4)3-FLAB**	**CE**	Although 3-FLAB is better than the other methods, none of the methods have given sensible results for lesions smaller than the size of 20 mm. **Error rates for overall tumors:** AT: 20±12% FCM: 17±14% FLAB: 15±11% 3-FLAB: 9±8%

Continued on next page

Table 2.1 – *Continued from previous page*

Literature Studies	Data	Segmentation Methods	Evaluation Metrics	Notes
Hatt et al. (2011) [19]	**1)Phantom Data:** Data consists of 6 spheres (Size: 10-37 mm, SBR: 4 and 8). / Voxel sizes: 2x2x2 mm^3 and 4.3x4.3x4.25 mm^3 / 4 scanner types / Rec: 3D RAMLA, TF ML-EM, and FORE-OSEM / Scan durations: 1, 2, and 5 min. **For repeatability study:** 1)Ten tumors obtained from realistically simulated PET scans. Voxel size: 4x4x4 mm^3. 2)Clinical images: 4 esophagus lymphomas 4 follicular lymphomas 3 NSCLC	**1)Manual Delineation** **2)Fixed Thresholding** (T42%, T50%) **2)Adaptive Thresholding** (Daisne's method) **3)FCM** **4)FLAB**	**CE**	The 10 mm sphere is excluded from the study because of the lower contrast. **Accuracy:** Mean of CE% **Robustness:** SD of CE% Repeatibility: To segment an image for several times. (This was done for only second dataset.) **1)For all spheres (13-37 mm):** The FLAB method is the most accurate and robust: 8.7±4.5%. The T42% method is the least accurate and robust: 42.6±51.6% **2) For repeatability study:** The AT, the FCM, and the FLAB methods showed good variability results (<5%) compared with manual delineation (5-35%).
Khamwan et al. (2012) [21]	**1)Nema IQ Phantom:** Phantom data consists of 6 spheres. (Size: 10-37 mm, SBR: 4, 8, 12, and 16) / Matrix size: 256x256 with 4 mm slice thickness / Rec: OSEM, 4 it, 8 subsets / 5 mm Gaussian smoothing / Siemens Biograph PET/CT Scanner / 3D acq. mode. **2)Clinical Data:** Clinical data includes ten patient images of oesophageal cancer.	**1)Manual segmentation** **2)Otsu's method** **3)Active contour with shifted optimal thresholding** (The proposed method) **4)Active contour without edges** (ACWE)	1)VE% 2)Dice coefficient (DC)	Volume errors are given with respect to various sphere sizes for the segmentation methods used. Their proposed method improved the accuracy and precision of the PET tumor delineation compared with others. For the proposed automated method, the following lists show the segmentation volume errors of the phantom spheres at SBR of 4. 10 mm lesion: 35% 13 mm lesion: 33% 17 mm lesion: 22.5% 22 mm lesion: 16.5% 28 mm lesion: 12.2% 37 mm lesion: 6.5%
Onoma et al. (2014) [24]	**1)Phantom Data:** 8 homogeneous spherical lesions (Volume: 0.99-97.3 mL, SBR: 2, 3.4, 4.9, 6,3, and 7.7) / Matrix size: 168x168x75 / Voxel size: 4.1x4.1x2 mm^3/ Rec: AWOSEM, 4 it, 8 subsets / Gaussian smoothing with the FWHM of 5 mm / FOV: 162 mm / spatial resolution: 6.8 at the center of the FOV. **2)Simulation Data:** 4 heterogenous spherical lesions (Size: 12, 29, 57, 90 mm). **3) Clinical Data:** 14 images of the patients with NSCLC. Medical experts classified the six lesions as homogenous (volume: 1.9-37.7 mL) while the rest as heterogenous (volume: 20.8-135.8 mL).	**1)Fixed Thresholding** (T40%) **2)Adaptive Thresholding** (AT) **3)FLAB** **4)Random Walk** (RW) **5)3D Locally Adaptive Random Walk** (3D-LARW): The proposed method	**1)VE%** **2)CE** **3)Jaccard Index** (JI)	**1)Phantom Results:** The best adaptive parameter is determined by comparing volume errors for the LARW method. The 3D-LARW is the best one for segmentation. The best VE% is obtained for the largest sphere (9.2±3.8%). For the smallest sphere, the VE% is 48.4±22.2%. **2)Simulation Data Results:** Similarly, the proposed method is the best compared to others. The CE%s are (10-20%) for the smallest one and (5-10%) for other lesions. **3)Clinical Data:** Overlap measurement of the segmented lesions is compared with the medical expert's delineation using the JI metric. For heterogeneous lesions, the proposed method showed statistically better results than the other methods. However, it is not statistically significant for the homogeneous lesions.

Continued on next page

Table 2.1 – *Continued from previous page*

Literature Studies	Data	Segmentation Methods	Evaluation Metrics	Notes
Prieto et al. (2012) [22]	**Phantom Data:** 6 homogeneous spherical lesions (Size: 10-31 mm, SBR: 2, 4, and 8) / 2 different PET Tomographs: Siemens PET/CT and Philips PET Scanners. **For the Siemens PET/CT Scanner:** Voxel size: 5.3x5.3x3.4 mm^3/ Matrix size: 128x128x47 / Rec: OSEM, 2 it, 8 subsets **For the Philips PET Scanner:** Voxel size: 1x1x1 mm^3/ Matrix size: 128x128x120 / Rec: 3D RAMLA	**1)Fixed Thresholding** (T42%) **2)Twelve automatic thresholding algorithms** which are based on clustering, histogram shape, object attribute, entropy, spatial information, and local image characteristics.	**1)VE% 2)CE 3)1-DSI**	Four of the twelve methods provided better results than the standard clinical thresholding algorithm (T42%). Three of these four methods are based on clustering: Ridler, Yanni, and Otsu. Another method, Ramesh, is based on the histogram shape characteristics of the image. Average results of the three metrics were given as 9.8, 10.1, 11, 16.4, and 18.9 for Ridler, Ramesh, Otsu, Yanni and the T42%, respectively.
Zaidi et al. (2012) [23]	**Clinical Data:** Clinical data consists of 7 patient images of the T3-T4 squamous cell carcinoma (including heterogeneous activity distributions). Images were acquired by Siemens PET Scanner. Image Reconstruction: 3D AW-OSEM with 8 it. and 4 subsets. Full correction steps are implemented for all images. The corrected data are denoised using 3D bilateral filter. The Landweber's iterative algorithm is used to deblur images after denoising step. The mean value of the tumors' volume is 15.15 mL (4.3-32.92 mL).	**1)Thresholding methods** (Black's, Biehl's, T40%, Nestle's, and Schaefer's method) **2)Active Contour Method 3)Stochastic Expectation 4)FCM 5)FCM-Spatial Wavelet Method** *(FCM-SW)*	**1)VE% 2)CE% 3)DSC**	**1)**All thresholding methods without Schaefer's method and the Expectation Maximization method overestimated the average lesion volume. **2)**The reference volumes are obtained from the histological specimens. The mean reference volume is 15.15 mL. **3)**The Schaefer's method underestimated the average volume. However, the error rate (-31.9%) is lower than the other thresholding methods. The FCM, active contour, and the FCM-SW methods provided better results than the others (35.6%, 27.2%, and -5.9%, respectively). **4)**The FCM-SW has the highest accuracy in terms of overlap measurement.
Zhuang et al. (2016) [26]	**1)Phantom Data:** A Cardiac-Torso (XCAT) Phantom consists of ten realistic tumors with heterogenous activity distributions. SBR: 8, 9, and 10. / Volume: 3.46-41.44 mL. / Matrix size: 288x288 / Voxel size: 2.13x2.13x3.27 mm^3 / Reconstruction: OSEM for the scanner type GE Discovery PET/CT. **2)Clinical Data:** It consists of 6 images of pharyngolaryngeal squamous cell carcinoma tumors and 10 images of NSCLC tumors. Lesion volumes ranged from 4.03 to 32.92 mL and 1.12 to 46.28 mL for the first and second data sets, respectively. Ground truth volumes are determined by surgically resected specimens. SBRs ranged from 2.2 to 21.1. The mean SBR value is 7.98±5.83.	**1)**Schaefer's Thresholding Method (ST) **2)**The Contourlet based Active Contour Algorithm (CAC) **3)**The Automatic Segmentation using Active Contour Method *(The proposed method: MASAC)*	**1)VE% 2)CE% 3)DSC**	The proposed method (MASAC) compared with the CAC and the ST method. **1)Phantom Results:** The ST method provided lower VE% but higher CE% compared to the other two methods. The MASAC and the CAC methods are more reliable than the ST method. VE%s are -8%, 17%, and 13% for the ST, the CAC, and the MASAC methods, respectively. In the same order, the DSCs are 0.76, 0.91, and 0.89; and the CE%s are 47%, 20%, and 19%. **2)Clinical Study Results:** The proposed method (MASAC) provided better results in terms of the DSC (0.71) and the CE% (54%). However, the CAC method is the best in terms of the VE% (8%).

2.2 Partial Volume Effect

In an ideal case, if we were able to eliminate all image degrading factors such as the limited spatial resolution of the system, the sampling grid size, noise, and motion; an image of the object would be as close as possible to its actual shape as shown in the Figure 2.1 (a). However, these degradations cause blurry edges and decrease the signal intensity and contrast of the object in the acquired image as illustrated in Figure 2.1 (b) and (c). Hence, a small object, whose size is smaller than 2 or 3 times the spatial resolution of the system, is seen as larger and weaker than it actually is. This phenomenon is known as the Partial Volume Effect (PVE) [5].

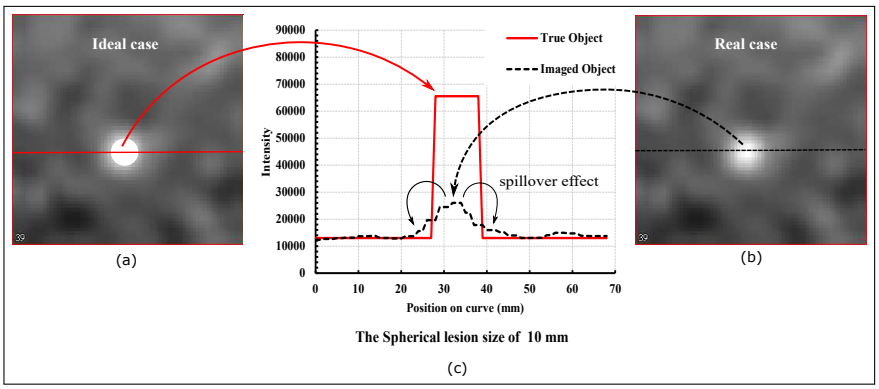

Figure 2.1 The intensity profile of the real object (ideal case) (a), and acquired image (real case) (b). Note that in real case, the intensity profile is seen as larger and weaker than it actually is due to the PVE (c).

A major reason for the PVE is the finite spatial resolution of the imaging system. PET scanner characteristics, designs, and PET reconstruction processes have led to inevitable distortions. If a cold object is placed into a hot background, some of the background signals spill into the object's region. Conversely, if a hot object is placed into a cold background, part of the object's signals spills out to the background regions as shown in Figure 2.1 (c). Indeed, this effect is basically a consequence of the limited spatial resolution of the scanner.

Another reason for the PVE is the limited sampling grid size. When a voxel of an image is represented by partially filled radiotracers from two or more regions such as tumor, lung, liver, and muscle tissues; mean signal intensity values of these regions

are assigned to their voxels. Therefore, signal intensities at these voxels are reduced by tissue fraction effect as illustrated in Figure 2.2. As far as pixel size and spatial resolution are concerned, anatomical imaging modalities are better than PET and SPECT imaging. However, this effect can cause some sort of quantitative measurement errors even for CT and MRI.

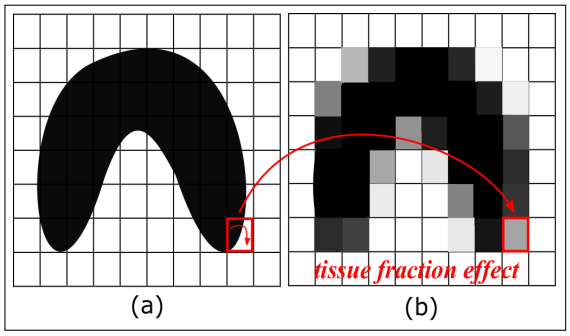

Figure 2.2 An ideal object (a), and its acquired image (b). Note that signal intensity is reduced due to the limited sampling grid size in (b) (tissue fraction effect).

Jomaa et al. [30], Erlandsson et al. [31], and Bettinardi et al. [32] presented comprehensive reviews of the PVE in PET tumor imaging. They investigated the causes of the PVE and explained the available Partial Volume Correction (PVC) methods.

PVC methods can be applied either during or post-reconstruction processes and classified into region and voxel-based correction techniques. Amongst the region-based methods, Recovery Coefficient (RC), which is the ratio of PET measured radioactivity concentrations to actual radioactivity concentrations, is a widely used technique [33]. Clinically, it is generally impossible to know actual radioactivity concentrations; so look-up table or other imaging modalities (CT and/or MRI) have been used for RC correction method. The other method used for more than 2 structures in images is the Geometric Transfer Matrix (GTM) correction. PVE has been corrected using this method either working with PET raw data in the sinogram or in the image domain [34].

Amongst the voxel-based correction methods, recovery of the spatial resolution of the system can be achieved using image reconstruction, deconvolution, multi-resolution approach, and anatomical imaging. Thus far, several studies have attempted to evaluate the impact of deconvolution techniques in terms of RC and Standardized

Uptake Value (SUV) during reconstruction or post-reconstruction process [35–42].

Rizzo et al. implemented Lucy-Richardson (LR) deconvolution to improve PET spatial resolution using a known PSF which was measured from the imaging system during the reconstruction process [35]. They concluded that using the LR deconvolution algorithm led to an improvement in image enhancement. However, they did not consider the optimum deconvolution parameters. Moreover, no quantitative results were emphasized in terms of measured volume.

Teo et al. used an iterative deconvolution technique based on Van Cittert's method. This method was conducted on the reconstructed images obtained from phantom, simulated, and clinical data [36]. A Gaussian function with the Full Width at Half Maximum (FWHM) of 6.5 mm was used for the PVC method. The efficiency of the method was measured using recovery coefficients. They determined the stopping iteration value of 4 using simulated data only without considering noise and background effects. In addition, they implemented a known PSF size (Gaussian function) with FWHM of 6.5 mm for the recovery process.

Tohka et al. used two types of PVC method (deconvolution-based and MRI-based PVC) on simulated data [37]. The data consisted of 16 simulated dynamic ^{11}C-Raclopride PET brain images. The performance of each correction method was compared in terms of bias and variance of the Binding Potential, Root Mean Square Error (RMSE) of the time-activity curves, Contrast Recovery Coefficient (CRC), and Coefficient of Variation (CoV). They found that the Reblurred Van Cittert deconvolution algorithm performed a better performance compared to others.

Kirov et al. used a post-reconstruction PVC method (3D MLEM algorithm) based on iterative deconvolution for phantom, simulated, and clinical data [38]. The performance of the correction method was examined using activity profiles and the mean CRC. Their method improved the quantification accuracy without increasing noise in the background. However, the method was not tested for large lesions with heterogeneous activity distributions.

Barbee et al. implemented the post-reconstruction based iterative PVC method on phantom and clinical data using expectation maximization algorithm with spatially variant and invariant PSF [39]. The performance of the correction method was tested using the RC method. They found that the spatially varying PVC method improved RCs. They used a known PSF in the correction method using a point source at various radial distances from the center of the scanner's Field of View (FOV).

Hoetjes et al. implemented reconstruction-based, image-based (Richardson-Lucy deconvolution and Van Cittert deconvolution), and mask-based PVC methods on phantom and simulated data [40]. The performance of the correction methods was examined using the RC and the SUV. All methods recovered true activity within 20% for phantom and simulated lesion volumes equal to and larger than 1 cc. The SUV improvement varied from 5% to 80% depending on the lesion volumes. The isotropic Gaussian PSF was used in the reconstruction process for the reconstruction-based method. This correction method indicated better performance compared to others.

Hatt et al. used iterative deconvolution (Richardson-Lucy) algorithms with wavelet denoising (Bayesshrink filter) on PET images [41]. The performance of the correction method was tested using SUV values (SUV_{max}, SUV_{mean}, and SUV_{peak}), Metabolically Active Tumor Volume (MATV), and Total Lesion Glycolysis (TLG). The MATV was measured using the FLAB method before and after the correction process. They reported that the PVC method increased all types of SUV values, but these differences are not statistically significant. Slight decreases were observed for the MATV and the TLG after the PVC method, but this alteration is not significant. In addition, they implemented the correction on large clinical lesions (40±30 cc) only.

In another study, Merlin et al. investigated the effect of the LR deconvolution algorithm using various denoising filters [42]. At first, LR deconvolutions with BayesShrink and BlockShrink methods were conducted on reconstructed phantom images. In the second step, the LR method with and without denoising was implemented before and after reconstruction using a measured PSF. Performance of the correction methods was measured with the Contrast Recovery (CR) and the Relative Standard Deviation

(RSD). Four small spheres of the reconstructed phantom data with SBR of 8:1 were deconvolved by using LR algorithm with and without denoising at 1, 3, 6, and 9 iterations. CR and RSD values showed that integrated LR method into the reconstruction with a known PSF performed better performance compared to others.

These studies have shown that iterative PVC methods with a known or measured PSF function improve resolution and contrast at the expense of increasing noise. However, these improvements were examined for specific types of lesions using only RC, activity profiles and/or SUV values. In the next section, the blind deconvolution method which uses an unknown object and a PSF function will be investigated for the restoration of PET images.

2.3 Image Restoration with Blind Deconvolution

A digital image is described mathematically as a combination of the real image, the PSF, and the noise. In other words, it is composed of the noise, and the convolution of the real image by the system's PSF as shown in Eq. 2.5, where $g(x, y, z)$, $f(x, y, z)$, $H(x, y, z)$, and $n(x, y, z)$ indicate respectively the blurred 3-D image, the real image, the PSF of the system, and the additive noise.

$$g(x, y, z) = f(x, y, z) * H(x, y, z) + n(x, y, z) \tag{2.5}$$

Image deconvolution is a restoration technique that recovers the real image from the blurred image with or without known information about the real image, the blurring factor of the imaging system, and the noise. Figure 2.3 displays a general image restoration procedure. Various techniques have been developed in order to restore undistorted images, such as no-neighbors methods, neighboring methods, linear methods, nonlinear methods, statistical methods, and blind deconvolution methods [43]. The iterative blind deconvolution method has extensive usage because of its computational simplicity and its robustness in the reduction of noise [44, 45].

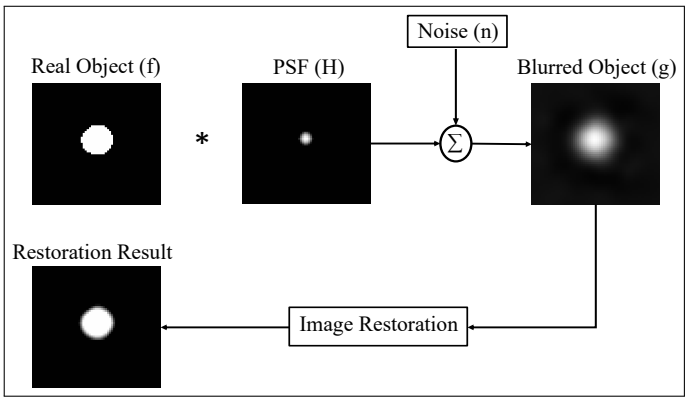

Figure 2.3 Schematic illustration of a general image restoration process.

Although the blind deconvolution has been widely used in microscopic and astronomical images, there has been limited use on medical images. In addition, few studies have examined the effect of the blind deconvolution method on segmentation accuracy of the PET lesions [46]. In their study, Guvenis et al. investigated the effects of the restoration on lesion delineation using four interactive methods and manual delineation. The present thesis includes 3D local deconvolution, resampling and is a continuation of an earlier work by the authors [46].

In another study, Li et al. applied integrated total variation semi-blind deconvolution and Mumford-Shah segmentation with multiple regularization methods on phantom and clinical data [47]. The proposed method was compared with various PET segmentation methods. Better performance was obtained for different sphere sizes and SBRs using phantom data. Similarly, better results were obtained for the non-Hodgkin's lymphoma and esophageal cancer lesions. Although their method performed better, high computational costs may be induced if there are more optimal solutions than one.

In another study, Koc et al. conducted image restoration in 3D lesions to compensate for blurring effects resulting from the PVE and used thresholding for tumor delineation on a limited phantom dataset [48]. Their results showed that the local blind deconvolution, together with resampling, improved the segmentation accuracy of small lesions. The computation time was also significantly reduced.

There remains a need for an additional study to find the most appropriate PET image segmentation method that can maximize segmentation accuracy for various lesion characteristics at a lower computational cost together with the best deconvolution parameters. To fill this gap, this thesis develops an alternative approach by combining post-reconstruction local deconvolution and resampling methods. Five segmentation techniques, Adaptive Thresholding (AT), Maximum Entropy Thresholding (MET), Region Growing (RG), Active Contour with Classification (ACWC), and Fuzzy C-Means Clustering (FCM) were used to quantify the lesion volumes of the phantom, simulated, and clinical PET images before and after the restoration.

The Region-of-Interest (ROI) and post-reconstruction approach to deconvolution may have several potential advantages over the deconvolution of the entire 3D image: First, the PSF is considered fixed only for a small region. Second, computational time may be reduced considerably due to a small volume deconvolution since only an ROI around the tumor can be considered in post-reconstruction. Third, deconvolution is carried out for any residual PVE that might remain after reconstruction for a particular tumor region. PSF estimation errors during reconstruction may also be avoided. Furthermore, it is expected that the best iteration number may be estimated using the highest Contrast to Noise Ratio (CNR). Therefore, by using both CNR and ROI based deconvolution, it is expected to significantly increase delineation accuracy while reducing computational time and implementation complexity. This may, therefore, lead to practical value in busy PET clinics.

3. MATERIAL AND METHODS

3.1 Data

In order to quantify the volume of the tumors, we drew upon three different datasets: the physical phantom, the simulated whole body ^{18}F-FDG PET oncology images, and the clinical patient data.

3.1.1 Dataset 1: The Phantom Data

To evaluate volume accuracy, a National Electrical Manufacturers Association image quality phantom (NEMA NU-2 IQ), containing six spheres with diameters of 10 mm, 13 mm, 17 mm, 22 mm, 28 mm, and 37 mm, was scanned by a GE Discovery STE-16 PET/CT scanner (16-row MDCT). Spheres and phantom were filled with Ge-68 concentration at fixed SBR of 4:1 with the initial background activity level set to be equivalent to 15 mCi in a 70 Kg patient. The activity level of the background and hot spheres were measured as 0.44 μCi/ml and 1.75 μCi/ml respectively. The phantom images were obtained using a 3D mode in a 5-minute acquisition with the reconstruction method, i.e., the 3D ordered subset expectation maximization (3D-OSEM) method with 28 subsets, 8 iterations, and 7 mm smoothing filter. The matrix size was 128x128x47 voxels for each image and the voxel size was 2.73x2.73x3.27 mm^3. The CT data of the phantom consisted of 63 slices with 512x512 pixels. Each voxel had a size of 0.68x0.68x2.5 mm^3. Detailed descriptions of the phantom images are available in the study of Clark et al. [49] and the reference [50].

Table 3.1 provides ground truth volumes (the nominal sphere volumes, the active epoxy volumes in spheres, and the manually segmented CT volumes) for spherical lesions of the phantom. These volumes are used as reference volumes to compare the efficiency of segmentation methods before and after the restoration process. Active

epoxy volumes and manually segmented CT volumes were used for volume measurement and overlap measurement, respectively. The central slices of the PET, CT, and manually segmented lesions are presented in Figure 3.1.

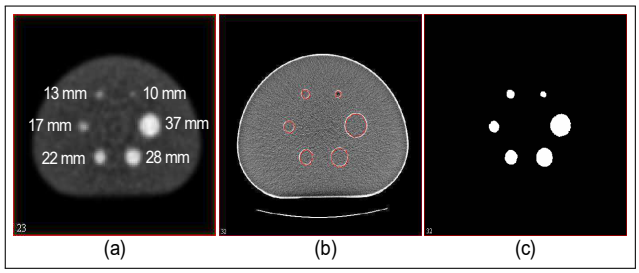

Figure 3.1 The central slices of the PET (a), CT (b), and manually segmented lesions (c). Note that volume measurement error of each segmentation technique is calculated before and after restoration with respect to reference volumes obtained from active epoxy volume values and manually segmented CT volumes.

Table 3.1
Ground truth sphere volumes of the phantom data.

Sphere sizes (mm)	Nominal volumes (mL)	Active epoxy volumes (mL)	Manually Segmented CT volumes (mL)
37	26.52	26.34	25.28
28	11.49	11.23	11.47
22	5.58	5.43	5.38
17	2.57	2.39	2.54
13	1.15	1.10	1.22
10	0.52	0.49	0.48

3.1.2 Dataset 2: The Realistic Simulated Whole Body ^{18}F-FDG PET Oncology Images

Another source of data was the realistic 3-D whole body ^{18}F-FDG PET oncology images obtained from the OncoPET_DB database [51, 52]. To begin with, a patient was modeled based on the Zubal phantom with activity concentrations in the interested organs acquired from a series of 70 clinical cases. Then, tumors were modeled as 3D spherical lesions of the real lymphoma patients. Finally, the realistic PET images were generated using the PET-SORTEO Monte Carlo simulation platform that was validated for the geometry of the ECAT EXACT HR+ scanner. Images were reconstructed

with the Attenuation-Weighted (AW)-OSEM algorithm using six iterations and 16 subsets; and are subsequently post-filtered with a Gaussian isotropic smoothing function of 8 mm. Each image had a voxel size of 5.0625x5.0625x2.425 mm^3 and a matrix size of 128x128x375 voxels. Lesions with diameters of 10.5 mm and 14 mm at two SBRs of 4:1 and 10:1 are illustrated in Figure 3.2. The performance of the segmentation algorithms after deconvolution was also evaluated using this dataset (worst-case scenario).

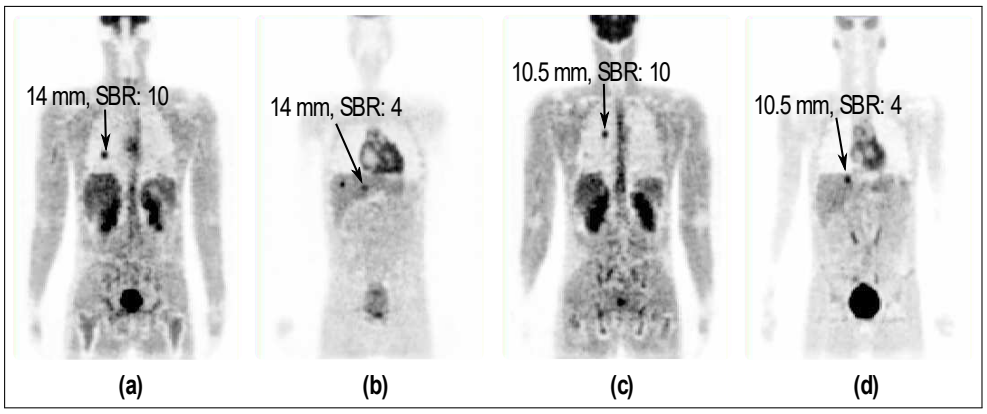

Figure 3.2 The coronal slices of 3-D whole-body ^{18}F-FDG PET images with the lesion size of 14 mm at SBR of 10:1 (a), the lesion size of 14 mm at SBR of 4:1 (b), the lesion size of 10.5 mm at SBR of 10:1 (c), and the lesion size of 10.5 mm at SBR of 4:1 (obtained from the reference [48]).

3.1.3 Dataset 3: Clinically Relevant Large Tumors with Irregular Shapes and Non-uniform Activity Distributions

The last source of PET/CT data was obtained from six patients of an oncology database [53]. This database was generated using the GATE Monte Carlo simulation platform based on the Philips PET/CT Allegro/Gemini scanner. NURBS based cardiac-torso (NCAT), and Zubal phantoms were used to create two realistic lung tumors, one lymphoma, three brain tumors inside relevant organs. Each data was acquired within two minutes of acquisition time per bed position, and resultant sinogram data were reconstructed using the STIR software with two iterations. The matrix size was 128x128x57 voxels with a voxel size of 4x4x3.15 mm^3. In addition, a Gaussian smoothing filter of 5 mm was implemented on images after the reconstruction step. All the simulated tumors had arbitrary shapes with heterogeneous activity distributions and thereby resembled clinical images. The tumor volumes of the six patients ranged

from 40.38 mL to 203.84 mL as shown in Table 3.2. The visual illustration of the six tumors and their ground truth masks are demonstrated in Figure 3.3.

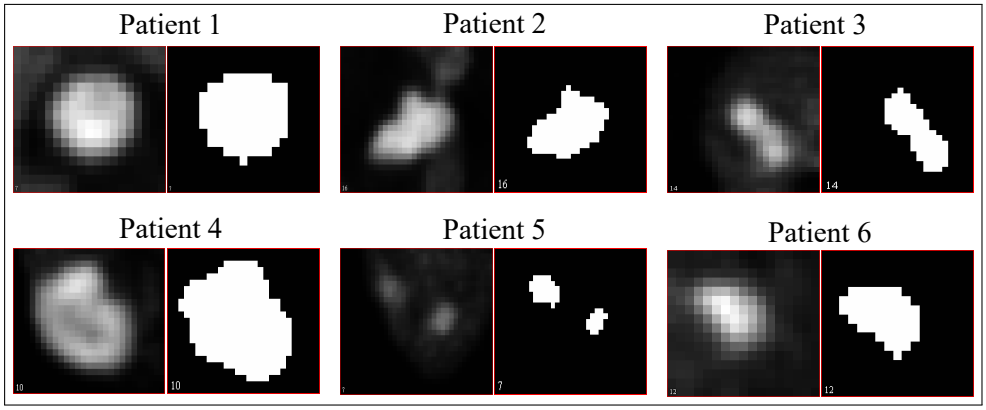

Figure 3.3 The visual illustration of the central slices in tumors and ground truth masks obtained from the Dataset 3.

Table 3.2
Ground truth volumes of the Dataset 3.

	Anthropomorphic models	**Tumor Regions**	**Tumor volumes (mL)**
Patient 1	NCAT	Lung	40.38
Patient 2	NCAT	Lung	203.84
Patient 3	Zubal	Lymphoma	65.6
Patient 4	Zubal	Brain	196.35
Patient 5	Zubal	Brain	53.89
Patient 6	Zubal	Brain	57.15

3.2 The Local Extraction Method: Cropping

The spatial resolution of the PET imaging system is the highest at the center of the scanner's FOV and deteriorates towards the edge of the FOV, i.e., the PSF spatially varies from center to the edge of the FOV [54]. Therefore, the tumor regions have been locally extracted to compensate for the spatially varying PSF. Table 3.3 presents the information of the extracted tumor regions.

Table 3.3
Physical properties of the locally extracted regions.

	Lesions	Extracted Regions (Voxels)	Voxel Sizes (mm^3)
Dataset 1	**37 mm**	25x25x25	2.73x2.73x3.27
	28 mm		
	22 mm		
	17 mm		
	13 mm		
	10 mm		
Dataset 2	**14 mm, SBR: 10**	15x15x25	5.06x5.06x2.43
	14 mm, SBR: 4		
	10 mm, SBR: 10		
	10 mm, SBR: 4		
Dataset 3	**patient 1**	19x16x15	4x4x4
	patient 2	32x26x34	
	patient 3	24x28x26	
	patient 4	27x23x20	
	patient 5	35x27x18	
	patient 6	17x16x25	

3.3 Resampling

In general, nuclear medicine images have a larger voxel volume than CT and MRI images. The real shape of a PET lesion and its activity distributions may be accurately recovered by matching resampled PET image voxels with its ground truth segmentation map of high-resolution anatomical images. In addition, it may be possible to avoid errors originating from the segmentation of non-cubic voxels in original images. Furthermore, the resampling process enables us to use various initial PSF kernels in the deconvolution process depending on varying spatial distortions. Therefore, a resampling step was added in order to obtain a finer version before deconvolution [55, 56]. This step also served to obtain cubical voxels using the trilinear interpolation method with the freely available MIPAV software [57, 58].

3.4 Blind Deconvolution

As shown in Figure 2.3, blind deconvolution is an image restoration technique that aims to recover the real image (f) from a noisy blurred image (g) when the blurring function (H) and the real image (f) are unknown. This restoration method was performed using the following MATLAB *deconvblind* function:

$$[J, PSF] = DECONVBLIND(I, INITPSF, NUMIT), \tag{3.1}$$

where J is the estimate of the real image (f), PSF is the final estimate of the blurring function (H), I is the blurred image (g), INITPSF is the initial estimate of the blurring function (H) of the system which is a 3-D array with the same class as the input image (I) containing values of 1, and NUMIT is the number of iterations needed [59]. The function restores the image (I) using the Accelerated Damped Lucy-Richardson Algorithm and iteratively estimates both the deblurred image J, i.e., the real image (f), and the PSF, i.e., the blurring function (H) [45, 60].

The output of the restoration process depends on the initial PSF size and the number of iterations. Each iteration includes two cycles, and each cycle includes a single Lucy Richardson step as shown in Figure 3.4.

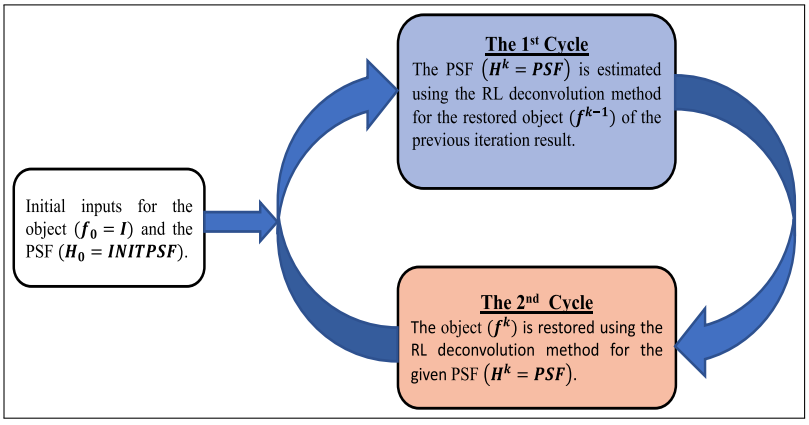

Figure 3.4 General iterative blind deconvolution method based on the Lucy-Richardson Algorithm.

In the first cycle, at k$^{\text{th}}$ iteration, a new PSF (H^k_{i+1}) is estimated from Eq.

3.2 using a restored object (f^{k-1}) and PSF (H_i^k) obtained from k-1 blind iteration and previous R-L iteration (i), respectively. In the second cycle of the same blind iteration (k), the true object (f_{i+1}^k) is estimated from Eq. 3.3 using the PSF (H^k) and the restored image (f_i^k) obtained from the output of the first cycle and previous R-L iteration (i), respectively. As a result, the loop is repeated to find best estimation of the true image (J), and the system blurring function (PSF) for a given iteration number (NUMIT).

$$H_{i+1}^k(x,y,z) = \left[\left(\frac{g(x,y,z)}{H_i^k(x,y,z) * f^{k-1}(x,y,z)}\right) * f^{k-1}(-x,-y,-z)\right] H_i^k(x,y,z). \quad (3.2)$$

$$f_{i+1}^k(x,y,z) = \left[\left(\frac{g(x,y,z)}{f_i^k(x,y,z) * H^k(x,y,z)}\right) * H^k(-x,-y,-z)\right] f_i^k(x,y,z). \quad (3.3)$$

Too many iterations may produce more ringing artifacts than less iterations and cause visually worse deblurred images. Therefore, the *edgetaper* function is used to reduce ringing artifacts before calling the *deconvblind* function. In the function, only two parameters (the initial PSF size (*INITPSF*) and the number of iteration (*NUMIT*)) were used to carry out the restoration process. Default values are used for all other parameters (*DAMPAR*, *WEIGHT*, and *READOUT*). The restored image is strongly affected by the size of the initial PSF and the number of iteration. The optimum initial PSF size and the iteration value used are explained in the following subsection.

3.4.1 Determination of the Initial PSF Size and the Iteration Value

In the PET Imaging system, the spatial resolution of the reconstructed images varies between FWHMs of 5 mm and 8 mm. If this spatial distortion function is assumed to be iso-gaussian, its FWHM equals to 2.35 times of σ, and about 99.7% of the PSF data falls into the tail size of 6σ on image grid domain. Therefore, the initial PSF sizes used in the restoration process were calculated using Eq. 3.4 for each FWHM of 5, 6, 7, and 8 mm. As a result, initial PSF sizes of 13, 15, 17, and 21 mm in 3 dimensions were obtained to subsequently be used in the deconvolution process for

each calculated amount of distortions of 12.8, 15.3, 17.9 and 20.4 mm, respectively.

$$\text{Initial PSF Size}(x, y, z) = 6 \cdot \frac{FWHM(x, y, z)}{2.35} \tag{3.4}$$

Once the initial PSF kernels were calculated, the restoration process was performed for a fixed iteration value of 1, and the best PSF kernel of each image was determined with respect to the highest CNR value. Then, the best number of iterations was found between varying iteration values (1, 2, 3, 4, 5, 7, 10, 15, 20, 30, 40, and 50) to arrive at the highest CNR value. The original and restored phantom lesions of 17 mm in size and their 3-D surface plots of the central slices are illustrated in Figure 3.5.

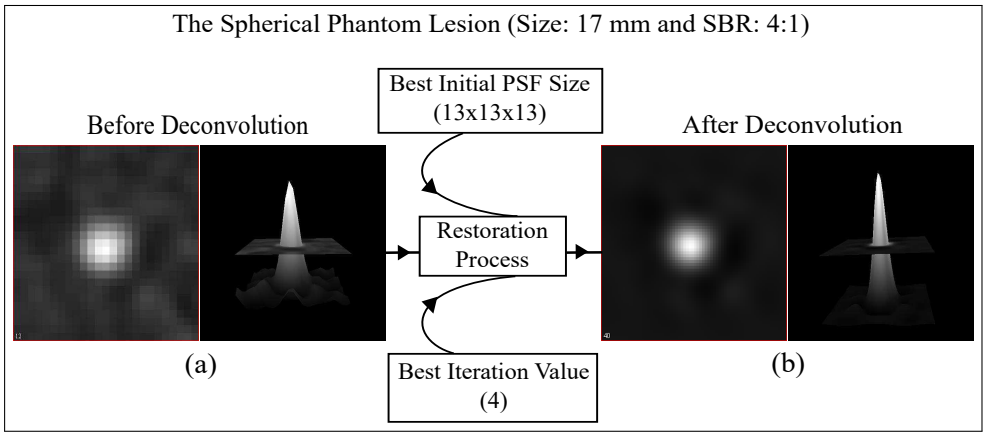

Figure 3.5 The central slice of the phantom lesion with size of 17 mm at SBR of 4:1 and its 3D surface plot before deconvolution (a), and after deconvolution (b).

3.5 Quantitative Evaluation Criterion for the Best PSF Size and Iteration Value

The best restoration can be achieved using optimum initial PSF sizes and iteration values. Determination of the PSF size and stopping iteration value may be problematic without the true image of the object. Therefore, CNR has been incorporated in our study to evaluate appropriate deconvolution parameters [60, 61].

As shown in Eq. 3.5, contrast component of each image was calculated by measuring the difference of the mean activity within the lesion volume of interest (VOI) (L_{mean}) and the background VOI (B_{mean}). The noise component (STD_B) was defined as the standard deviation of the activity within the background VOI.

$$CNR = \frac{L_{mean} - B_{mean}}{STD_B} \tag{3.5}$$

The lesion VOI and the background VOI were formed automatically using the level-set algorithm of the MIPAV software [58, 62]. While the lesion VOI was set to completely cover the lesion, the background VOI covered background regions around the lesion as shown in Figure 3.6.

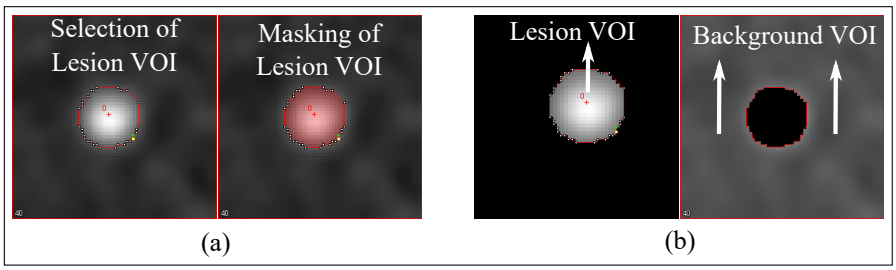

Figure 3.6 The lesion VOI was selected on the central slice of the phantom lesion with size of 17 mm at SBR of 4:1 (a), and a 3-D lesion VOI and a 3-D background VOI were formed to evaluate convergence rate of the deconvolution processes (b).

As previously stated, the performance of the deconvolution process highly depends on two parameters (the initial PSF size and the iteration value). Best parameter values were determined by comparing the experimental results of the CNR obtained from the original and restored images. The following steps summarize how the best deconvolution parameters were determined experimentally by using CNR method for each lesion.

- First, the lesion VOI which covers the entire lesion was generated automatically using the level-set contouring method of the MIPAV software on the central slice of the original resampled image.

- Second, the minimum pixel intensity of this lesion VOI was determined and then used as a threshold level for further 3-D segmentation of the lesion and background regions.

- After the segmentation process, 3-D lesion and background masks were constructed and used as support regions to evaluate CNR values of the original and restored images for varying parameters, i.e., these maps are frozen and used as the fixed support regions to evaluate the amount of enhancement on the restored images for each PSF kernel and iteration value.

- Then, the best PSF kernel was first determined in terms of the highest CNR value for a fixed iteration value of one as shown in Table 3.4.

- Finally, the best iteration number was found using the highest CNR value for fixed support regions as presented in Table 3.6. The CNR value increased up to the highest level with increasing iteration and then started to decrease after a certain level. For each lesion, the point where the reduction began was recorded as the best threshold for the iteration.

Table 3.5 summarizes the parameters measured and the experimental results of the CNR obtained from the original and restored images. These results indicate that for all datasets, CNR increases after deconvolution. Higher CNR is known to be a factor in segmentation accuracy [63]. In the next section, the effect of the deconvolution on segmentation accuracy was investigated using various PET segmentation methods.

Table 3.4
CNR values of the original and restored images at fix iteration value of 1.

		Original and Deconvolved Images				
	Lesions	**Original image**	**PSF (13x13x13)**	**PSF (15x15x15)**	**PSF (17x17x17)**	**PSF (21x21x21)**
Dataset 1	**37 mm**	13.55	20.99	21.25	21.40	**21.44**
	28 mm	12.68	22.55	22.73	**22.75**	22.39
	22 mm	11.54	24.38	**24.52**	24.43	23.62
	17 mm	10.01	**21.76**	21.68	21.34	20.26
	13 mm	8.09	**18.65**	18.30	17.83	16.88
	10 mm	4.99	**11.05**	10.64	10.24	9.65
Dataset 2	**14 mm, SBR: 10**	8.53	13.07	13.21	**13.21**	12.88
	14 mm, SBR: 4	5.29	8.29	**8.31**	8.27	8.05
	10 mm, SBR: 10	4.28	7.64	7.76	**7.76**	7.49
	10 mm, SBR: 4	4.52	7.59	**7.59**	7.51	7.25
Dataset 3	**patient 1**	5.30	7.73	7.76	7.81	**7.93**
	patient 2	7.74	9.33	9.37	9.40	**9.45**
	patient 3	5.43	6.87	6.92	6.97	**7.05**
	patient 4	9.41	12.21	12.50	12.78	**13.28**
	patient 5	7.82	9.70	9.87	10.04	**10.33**
	patient 6	6.41	8.39	8.51	8.61	**8.75**

Table 3.5
Best parameter and CNR values for various lesions.

				CNR	
	Lesions	**PSF Size (voxels)**	**Iteration Number**	Original	Restored
Dataset 1	**37 mm**	21x21x21	2	13.55	22.04
	28 mm	17x17x17	3	12.68	25.12
	22 mm	15x15x15	3	11.54	26.83
	17 mm	13x13x13	4	11.01	24.52
	13 mm	13x13x13	7	8.09	23.35
	10 mm	13x13x13	10	4.99	15.27
Dataset 2	**14 mm, SBR: 10**	17x17x17	15	8.53	21.92
	14 mm, SBR: 4	15x15x15	15	5.29	11.74
	10 mm, SBR: 10	17x17x17	15	4.28	15.27
	10 mm, SBR: 4	15x15x15	20	4.52	13.03
Dataset 3	**patient 1**	21x21x21	1	5.30	7.93
	patient 2	21x21x21	2	7.74	9.51
	patient 3	21x21x21	3	5.43	7.18
	patient 4	21x21x21	2	9.41	13.95
	patient 5	21x21x21	3	7.82	10.91
	patient 6	21x21x21	3	6.41	9.44

Table 3.6
CNR values of the original and restored images at various iteration values for given best PSF kernels.

		Original and Deconvolved Images												
	Lesions	**Original image**	**1 it.**	**2 it.**	**3 it.**	**4 it.**	**5 it.**	**7 it.**	**10 it.**	**15 it.**	**20 it.**	**30 it.**	**40 it.**	**50 it.**
Dataset 1	**37 mm**	13.55	21.44	**22.04**	21.35	20.18	19.03	17.25	14.31	10.18	8.01	5.59	4.21	3.57
	28 mm	12.68	22.75	24.35	**25.12**	24.90	24.23	22.42	19.46	15.01	12.33	9.98	7.80	5.91
	22 mm	11.54	24.52	26.02	**26.83**	26.71	26.09	24.20	21.30	16.86	13.23	9.02	6.86	5.67
	17 mm	10.01	21.76	23.05	24.13	**24.52**	24.43	23.47	21.32	17.69	14.81	11.31	9.11	7.69
	13 mm	8.09	18.65	19.87	21.19	22.14	22.77	**23.35**	22.93	20.56	17.76	13.51	10.95	9.31
	10 mm	4.99	11.05	11.85	12.79	13.57	14.19	14.98	**15.27**	14.49	13.24	10.96	9.53	8.55
Dataset 2	**14 mm, SBR: 10**	8.53	13.21	14.45	15.91	17.17	18.28	19.98	21.45	**21.92**	21.12	18.45	17.13	16.54
	14 mm, SBR: 4	5.29	8.31	8.92	9.55	10.09	10.55	11.22	11.71	**11.74**	11.38	10.50	9.56	8.49
	10 mm, SBR: 10	4.28	7.76	8.79	9.91	10.79	11.56	12.88	14.24	**15.27**	15.14	13.79	12.87	12.00
	10 mm, SBR: 4	4.52	7.59	8.22	8.89	9.47	9.99	10.87	11.83	12.71	**13.03**	12.75	12.34	12.04
Dataset 3	**patient 1**	5.30	**7.93**	7.84	7.62	7.44	7.28	6.92	6.54	6.23	5.92	5.09	4.58	4.27
	patient 2	7.74	9.45	**9.51**	9.48	9.40	9.29	9.07	8.74	8.27	7.86	7.18	6.69	6.32
	patient 3	5.43	7.05	7.17	**7.18**	7.13	7.06	6.92	6.69	6.31	5.93	5.12	4.56	4.23
	patient 4	9.41	13.28	**13.95**	13.88	13.28	12.55	7.13	6.01	4.66	3.82	7.79	8.23	0.00
	patient 5	7.82	10.33	10.78	**10.91**	10.81	10.60	10.10	9.39	8.46	7.74	6.95	6.32	5.82
	patient 6	6.41	8.75	9.21	**9.44**	9.42	9.26	8.74	7.72	6.46	5.77	4.96	4.34	3.86

3.6 Segmentation Methods

In section 2.1, a brief overview of the relevant literature on PET image segmentation techniques was reviewed and explained. As was mentioned in section 2.1, PET image segmentation methods have been classified as manual, thresholding-based, stochastic and learning-based, region-based, boundary-based, and joint segmentation methods. Different segmentation algorithms representing these classes have been selected for measurement of all original and restored volumes. The AT and the MET were used to represent a group of thresholding-based segmentation method, the RG was implemented to represent a group of region-based segmentation method, and the ACWC and the FCM method were used to represent a group of stochastic and learning based segmentation method. The AT, the MET, the RG, and the FCM clustering method were applied using the MIPAV software [62]. The ACWC method is based on the operation principle of Random Forests algorithm provided in the ITK-SNAP software [64, 65].The following subsections explain these segmentation methods and their implementation procedures in detail.

3.6.1 Adaptive Thresholding Method

The literature cites three types of threshold selection methods: fixed, adaptive, and iterative thresholding method. The SUV value of 2.5 and the 40 - 50% of the SUV_{max} value are the most widely used thresholding values within the fixed thresholding method. However, there is no consensus among researchers on using a particular thresholding method. Therefore, several groups of researchers have attempted to find the optimum threshold value in adaptive and iterative ways.

We implemented the AT method on original and restored images using Eq. 3.6. A threshold level for each lesion was found by calculating 42% of the difference of mean voxel intensities of lesion and background regions,

$$Threshold = (L_{mean} - B_{mean}) * 42\% + B_{mean}, \tag{3.6}$$

where L_{mean} is the mean intensity of the lesion VOI, and B_{mean} is the mean intensity of the background VOI. If the threshold percentage cannot be adjusted for foreground and background regions, it may be inappropriate in particular for small lesions. Therefore, in an attempt to determine small target volume (< 20 mm) 42% of the mean intensity difference was substituted by 50%. The calculated threshold values for segmentation of the lesions are displayed in Table 3.7.

Table 3.7
Threshold intensity values for adaptive segmentation algorithm.

		Threshold Values	
	Lesions	**Original images**	**Restored images**
Dataset 1	**37 mm**	23017	24689
	28 mm	21658	23732
	22 mm	20068	22277
	17 mm	20079	23691
	13 mm	19820	25570
	10 mm	17534	23713
Dataset 2	**14 mm, SBR: 10**	4058	8397
	14 mm, SBR: 4	12658	17756
	10 mm, SBR: 10	4143	9666
	10 mm, SBR: 4	12633	20755
Dataset 3	**patient 1**	0.155	0.164
	patient 2	0.445	0.471
	patient 3	0.087	0.099
	patient 4	0.135	0.140
	patient 5	0.078	0.092
	patient 6	0.160	0.177

3.6.2 Maximum Entropy Thresholding

The MET depends on the entropy of the histogram. It maximizes the entropy between the lesion (white pixels) and the background (black pixels). An image is divided into two classes (lesion and background) using the calculated threshold level. If an image consists of N pixels, i=1,2,.....,N, with gray levels (g_i), then the entropy of

each region is calculated separately with normalized histogram using Eq. 3.7.

$$H = -\sum_{i=1}^{N} \frac{g_i}{\sum_{i=1}^{N} g_i} log \frac{g_i}{\sum_{i=1}^{N} g_i} \tag{3.7}$$

Finally, the optimum threshold level is determined by maximizing the entropy of these two classes [66]. For all original and restored images, automatic threshold selection and segmentation processes were performed using the MIPAV software.

3.6.3 Region Growing Method

Region growing is a simple and flexible method based on the evaluation of the gray level of pixels or other characteristic properties of the local structures. The algorithm starts with a manually placed starting seed point, and segments pixels regarding homogeneity conditions of neighborhood pixels, i.e., it basically depends on the homogeneity and the seed point. The segmented region must have greater homogeneity than its boundaries in order to be segmented successfully. If more than one lesion will be segmented in an image, several seed points have to be placed in interested regions.

In this part, MIPAV software was used to segment the lesions in original and restored images. To perform the segmentation process automatically, two operations were performed. First, a seed point was defined on the image before segmentation. Then, the growing criterion from this seed point to edges of the image was determined. The center of mass value (seed point) of each lesion was calculated using the minimum threshold intensity values obtained from Table 3.7. All seed points acquired from the center of mass calculation are illustrated in Table 3.8.

Limiting the growing regions from these seed points is crucial for accurate segmentation of the lesion VOI. Generally, it has been achieved manually by setting upper and lower limits of the pixel intensities. Using a narrow range of intensity levels may cause underestimated lesion volume. Conversely, high-intensity intervals may cause overestimated lesion VOI. Therefore, varying delta values which changed according to

Table 3.8
Measured seed point locations in pixels and intensities for original and restored images.

		Original Images		Restored Images	
	Lesions	**Seed Locations**	**Intensity**	**Seed Locations**	**Intensity**
Dataset 1	**37 mm**	11x12x11	55881	32x34x38	77716
	28 mm	12x10x11	50013	33x27x38	85213
	22 mm	12x11x11	46374	33x30x38	81220
	17 mm	11x12x12	40123	32x34x39	71890
	13 mm	12x11x12	36378	32x32x39	67995
	10 mm	**outside the lesion**	**13081**	**32x40x38**	**45677**
Dataset 2	**14 mm, SBR: 10**	7x5x11	5703	40x29x28	28898
	14 mm, SBR: 4	7x6x11	18427	37x33x28	41409
	10 mm, SBR: 10	**outside the lesion**	**4708**	**36x32x29**	**25834**
	10 mm, SBR: 4	7x6x11	16201	37x36x27	46229
Dataset 3	**patient 1**	9x7x6	0.415	38x29x26	0.542
	patient 2	14x13x20	1.176	59x53x83	1.280
	patient 3	14x16x15	0.203	56x63x58	0.236
	patient 4	12x10x9	0.392	49x40x39	0.340
	patient 5	20x12x10	0.267	81x50x40	0.397
	patient 6	7x6x13	0.506	29x24x52	0.720

the growing region were drawn upon using the software feature. Figure 3.7 presents visual illustrations of the seed points' locations and segmented regions of the lesion size of 17 mm for original and restored images.

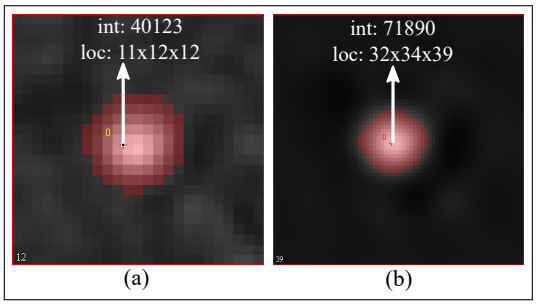

Figure 3.7 Seed point selection and 3-D region growing segmentation of the spherical phantom lesion with size of 17 mm at SBR of 4:1 for original image (a), and restored image (b).

3.6.4 Active Contour with Classification Method

Active contour with classification method is a semi-automatic segmentation technique which consists of two stages: the pre-segmentation phase and active contour phase. The first phase addresses the supervised learning method (classification process) in which the speed image has been generated from the given input image before active contour segmentation. In the second phase, 3-D segmentation of the lesion has been accomplished using the active contour method. These two methods and segmentation procedures are explained in the following two paragraphs.

In the classification process, lesion and normal tissues were defined manually with a closed contour on the given image for mapping unknown regions as shown in Figure 3.8 (b). Afterward, Random Forests classification method was implemented for defined regions to produce speed image with intensities in a range [-1,1] as illustrated in Figure 3.8 (c) and (d). The white color region represents lesion voxels, and the blue color region represents background voxels, i.e., voxels of healthy tissues in the speed image. After completing this pre-segmentation phase, the 3-D segmentation process is completed with the evolution of the placed contour in the lesion VoI.

The second step of the segmentation process starts with initialization, i.e., the 3-D contour is placed on the lesion VoI in the speed image and proceed to initialize evolving contour as displayed in Figure 3.8 (d). The initial contour moves in an image under the influence of the internal and external forces according to the Caselles et al. formulation as shown in Eq. 3.8

$$F = \alpha g_I - \beta \kappa g_I - \gamma(\nabla g_I \vec{N}), \tag{3.8}$$

where the first term, αg_I, is the outward direction force; κ is the mean curvature of the contour; g_I is the speed function; α, β, and γ are weights; $\vec{N}$ is the unit vector normal to the contour; and the last term, $\gamma(\nabla g_I \vec{N})$, is the inward direction force [67].

Evolution of the initialized contour was iteratively executed and controlled by

setting up parameters, $\alpha = 1$, $\beta = 0.2$, and $\gamma = 0$, as illustrated in Figure 3.8 (e) and (f). After completing the contour evolution step, the 3-D volume of the lesion was measured. These two methods and segmentation maps have been carried out using the ITK-SNAP software with Random Forests algorithm [65, 68].

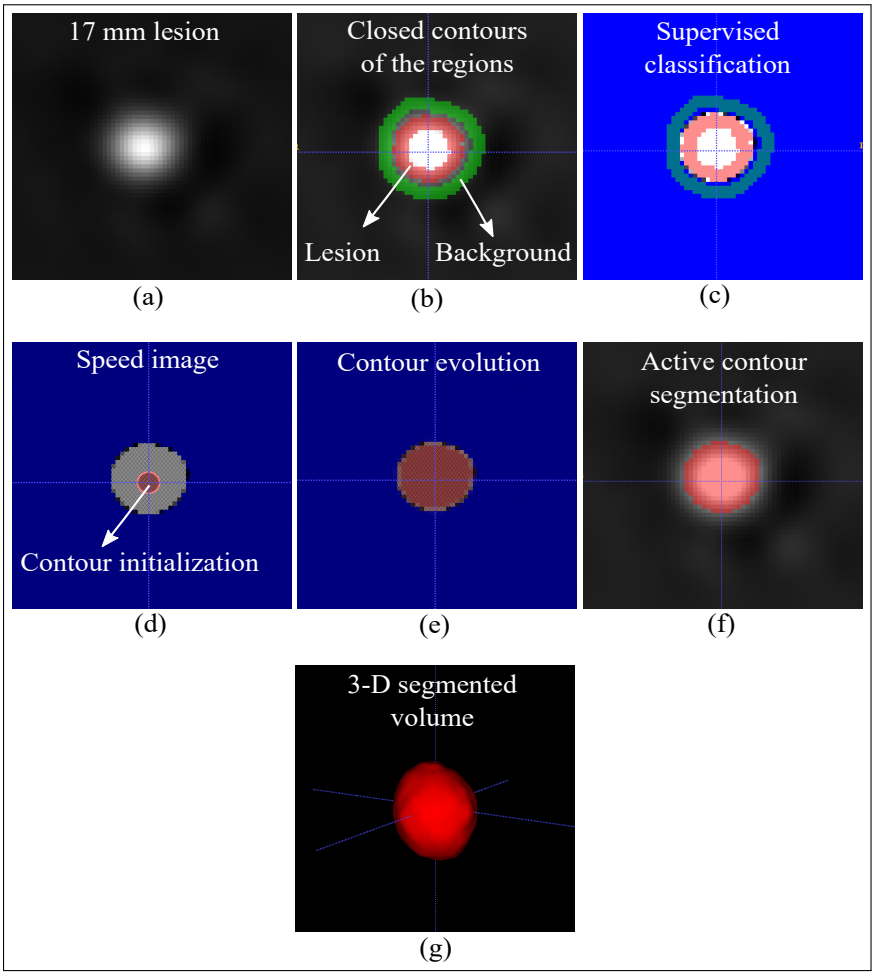

Figure 3.8 Active contour segmentation with classification method of the spherical phantom lesion with size of 17 mm at SBR of 4:1 for the restored image.

3.6.5 Fuzzy C-Means Segmentation Method

The Fuzzy C-Means segmentation is an unsupervised method which uses only input sample without training data. This method identifies the centroid of each cluster iteratively by minimizing the weighted distance between the observed data and its

cluster center as shown in Eq. 3.9,

$$J = \sum_{k\in\Omega} \sum_{i=1}^{c} \mu_{ik}^{q} \left\| x_k - v_i \right\|^2, \tag{3.9}$$

where μ_{ik}^{q} is a membership value at pixel location k for class i, q is the weighting factor that controls the influence of the membership values on the result, x_k is the observed intensity at location k, v_i is the center of the cluster i, c is the number of the clusters, and $\|x_k - v_i\|^2$ is a distance measure between the object x_k and the centroid v_i [62,69].

The FCM segmentation consists of four steps. The first step of the segmentation involves determination of the number of desired classes c, the weighting factor q, the limiting value $\in$, and the initial assignment of the membership function μ_{ik}^{q}. When the smaller q is chosen, it causes the membership value to be less effective in classification and leads to sharper segmentation results. In practice, the value of 2 is usually chosen for q. In our study, input images were locally extracted from whole images and included only lesion and background regions. Therefore, both the number of classes and the desired exponent value were chosen as 2. The limiting value is the end tolerance level which indicates when convergence is reached. The default value of 0.01 was selected for segmentation of all datasets.

In the second step, the algorithm calculates the centroid of the clusters, v_i, using membership values as shown in Eq. 3.10 for the single channel case.

$$v_i = \frac{\sum_{k\in\Omega} \mu_{ik}^{q} x_k}{\sum_{k\in\Omega} \mu_{ik}^{q}} \tag{3.10}$$

The third step involves updating the membership function (μ_{ik}^{q}) according to the rule for all objects that do not match a cluster center ($x_k \neq v_i$):

$$\mu_{ik} = \frac{\left\| x_k - v_i \right\|^{-\frac{2}{q-1}}}{\sum_{j=1}^{c} \left\| x_k - v_j \right\|^{-\frac{2}{q-1}}}; \tag{3.11}$$

otherwise, algorithm sets the value of the membership function to 0 if i is not equal to

j, and 1 if i is equal to j.

In the final step, the difference between two fuzzy partition matrices of the successive loops was determined to evaluate changes in the assignment of the objects to the cluster centers. If the difference is below a defined limit value $\in$, then the algorithm stops, otherwise, a new iteration is started. The main weakness of this algorithm is the huge computational effort. Therefore, when using this algorithm, the number of objects and the number of features should not be too large.

3.7 Error Evaluation Metrics

Evaluation of the segmentation plays a key role in choosing the right segmentation method and optimum parameters for a particular task. Various figures of merit have been developed and used by researchers in the literature and they are explained in section 2.1.5. The volume estimation accuracy and the overlap measurement of the segmented lesions were analyzed using the volume error percentage (VE%) and the Jaccard Index (JI), respectively [21, 24]. The VE% calculates the absolute percentage error of the volumes between segmented and ground truth images as displayed in Eq. 2.2. It takes the value of 0 when the volume of the segmented image is equal to the volume of the ground truth image.

On the other hand, segmented regions may not coincide with ground truth regions even if they have equal volumes. In such cases, it is necessary to use Eq. 3.12,

$$JI = \frac{TP}{TP + FP + FN}, \tag{3.12}$$

where TP indicates the ground truth voxels which are correctly classified as segmented lesion voxels, FP shows background voxels which are incorrectly assigned as segmented lesion voxels, and FN represents ground truth voxels which incorrectly belong to background voxels as illustrated in Figure 3.9. The JI value of 1 shows totally overlapped regions, while the value of 0 indicates completely non-overlapping regions.

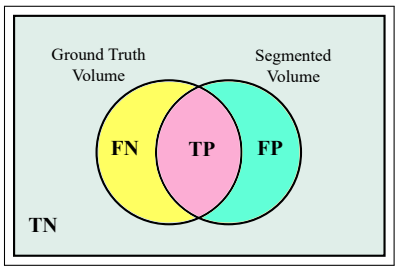

Figure 3.9 Overlap measurement method for segmented and ground truth voxels.

3.8 Structure of the Study

The study consists of two main parts. The first part addresses the segmentation of the lesion volumes obtained from the first, second, and third datasets. In the second part, the blind deconvolution method was implemented on resampled images which were locally extracted from original data, after which the volume of each lesion was compared with its ground truth. Figure 3.10 summarizes the methodology of our study.

3.9 Statistical Analysis

We used the two-tailed paired sample t-test for evaluation of the effect of the restoration on the PET segmentation methods. To examine where the differences occur, two combinations of related groups were used for each segmentation technique, i.e. segmented original volumes versus ground truth volumes on the one hand, and segmented restored volumes versus ground truth volumes on the other hand. All analyses were carried out using SPSS version 23 [70].

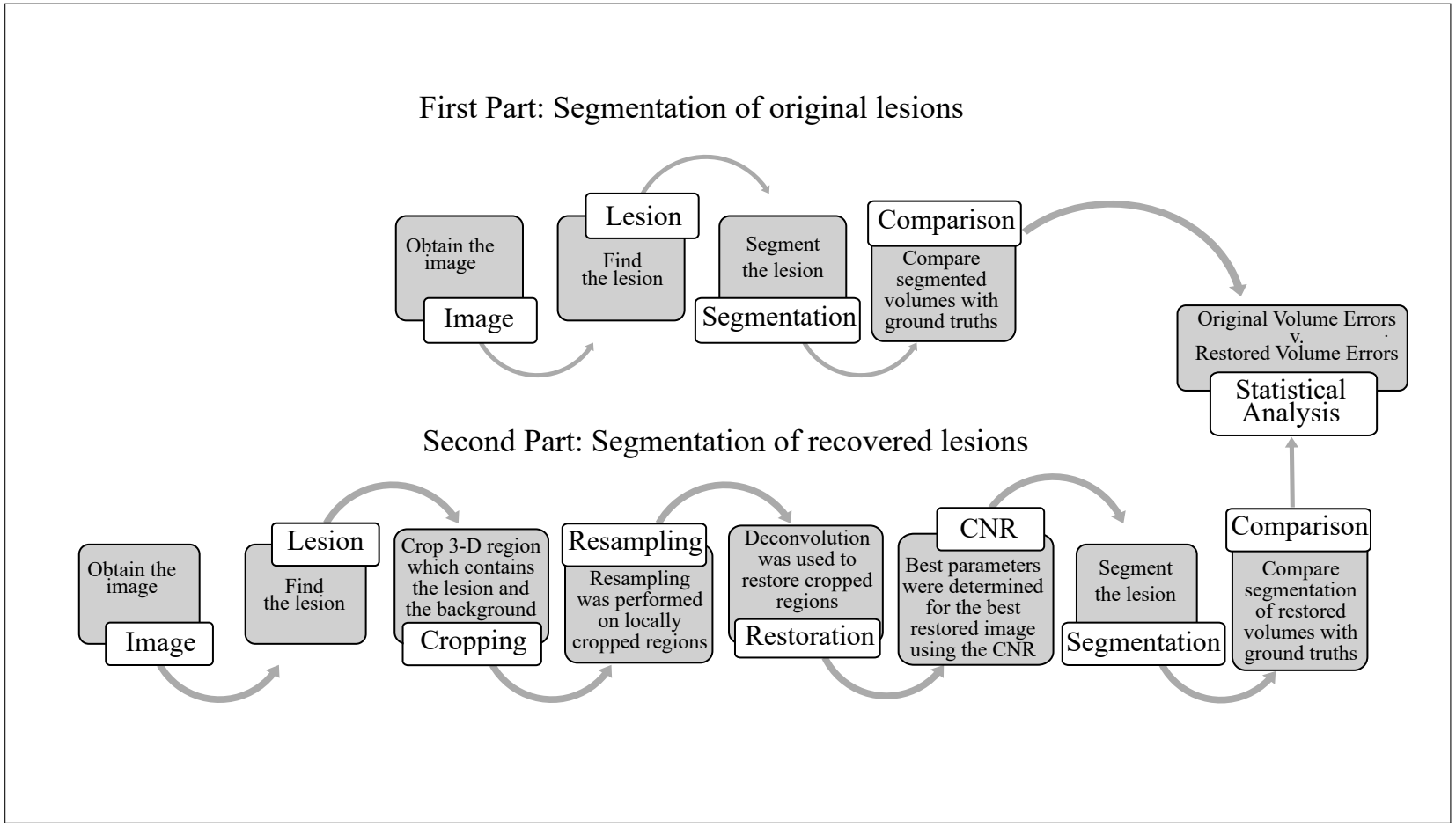

Figure 3.10 The methodology of our study.

4. RESULTS

4.1 Results of the Phantom Data

Six spheres of phantom data were recovered using the ROI-based blind deconvolution and resampling method. After the restoration process, all original and restored spherical lesions were segmented using various segmentation methods, and resulting volumes were compared with real volumes to assess the effect of this restoration on volume measurements. The degree of conformity (accuracy) and consistency (precision) between segmented and real volumes of each segmentation method was evaluated for both original and recovered images. The volume measurement results with respect to segmentation techniques used are presented in Table 4.1. The top half of the table shows measured volume values of the phantom lesions for each segmentation method, and the bottom half of the table shows their volume error percantages (accuracy and bias) and standard deviations (precision).

The mean volume error percentages reflect how accurately the segmentation is performed, while standard deviations indicate how precise it is. With the ROI-based blind deconvolution and resampling, the accuracy was improved in VE% by a factor of about 28.4 for the ACWC, 16.1 for the RG, 8.6 for the MET, 3.4 for the AT, and 1.5 for the FCM as illustrated in Figure 4.1. In the same way, the precision was improved in VE% by a factor of about 18.4 for the ACWC, 18.8 for the RG, 2.7 for the MET, 2.5 for the AT and the FCM segmentation methods as shown in Figure 4.1. The ACWC achieves a lower mean relative error of 3.37%±SD of 4.49% (minimum: 0.04%, maximum: 11.18%) compared with the result of other segmentation methods for recovered images.

Table 4.1
Segmentation results and absolute percentage errors of the Dataset 1 with respect to various segmentation techniques for original and restored cases.

	Segmentation Methods										
	AT		**MET**		**RG**		**ACWC**		**FCM**		
Lesions	**Orig.(cc)**[1]	**Dec.(cc)**[2]	**Orig.(cc)**	**Dec.(cc)**	**Orig.(cc)**	**Dec.(cc)**	**Orig.(cc)**	**Dec.(cc)**	**Orig.(cc)**	**Dec.(cc)**	**G. Truth (cc)**[3]
37 mm	31.52	28.32	36.14	27.16	36.82	26.30	33.91	27.09	24.99	20.70	26.34
28 mm	14.65	12.34	17.95	10.78	19.31	9.71	16.97	11.45	11.22	8.32	11.23
22 mm	8.12	6.66	9.63	5.51	11.71	4.78	8.75	5.39	6.19	4.34	5.43
17 mm	3.47	2.55	4.38	2.26	9.41	2.23	4.84	2.39	3.20	2.19	2.39
13 mm	1.76	1.24	2.49	1.44	-	1.58	3.69	0.98	1.76	1.12	1.1
10 mm	-[4]	0.61	1.10	0.77	-	1.86	0.93	0.69	-	0.73	0.49
Mean±SD	11.90±12.05	**10.22±11.00**	14.12±13.69	**9.43±10.57**	19.31±12.41	**8.92±10.23**	13.63±12.47	**9.46±10.65**	9.47±9.40	**7.33±7.97**	**9.30±10.30**
Lesions	**Orig.(VE%)**[5]	**Dec.(VE%)**[6]	**Orig.(VE%)**	**Dec.(VE%)**	**Orig.(VE%)**	**Dec.(VE%)**	**Orig.(VE%)**	**Dec.(VE%)**	**Orig.(VE%)**	**Dec.(VE%)**	
37 mm	19.65	7.52	37.19	3.10	39.79	0.16	28.74	2.85	5.14	21.40	
28 mm	30.41	9.87	59.80	3.98	71.99	13.52	51.11	1.97	0.07	25.93	
22 mm	49.48	22.67	77.40	1.40	115.67	11.92	61.20	0.83	13.90	20.17	
17 mm	45.27	6.69	83.11	5.65	293.85	6.74	102.55	0.04	34.02	8.54	
13 mm	60.00	12.91	126.71	30.64	-	43.45	235.64	11.18	60.00	1.91	
Mean±SD	40.96±15.96	**11.93±6.47**	76.84±33.13	**8.95±12.22**	130.33±113.36	**8.08±6.02**	95.85±82.60	**3.37±4.49**	22.63±24.58	**15.59±9.98**	

[1]The segmented volume of the original spherical phantom lesion is denoted by Orig.(cc).

[2]The segmented volume of the restored spherical lesion is denoted by Dec.(cc).

[3]The reference, ground truth volumes, of the spherical lesions is denoted by G. Truth (cc).

[4]The lesion could not be segmented with the specified method.

[5]Orig.(VE%) denotes the percentage volume error of the original spherical phantom lesion and calculated using Eq. 2.2.

[6]Dec.(VE%) denotes the percentage volume error of the restored spherical phantom lesion and calculated using Eq. 2.2.

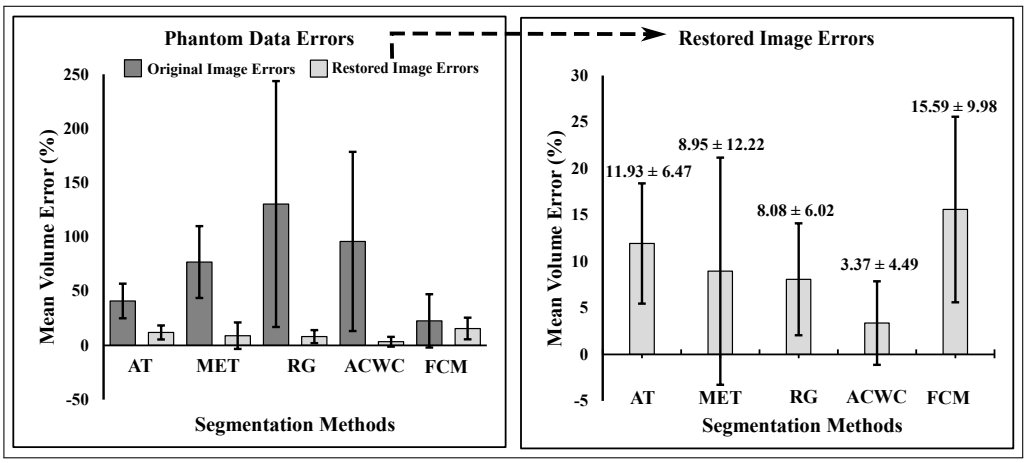

Figure 4.1 Mean absolute volume errors of the segmentation methods for original and restored phantom images (Dataset 1).

The mean value of the ground truth volumes is 9.30 cc (ranging from 1.1 cc to 26.34 cc). The smallest lesion (10 mm) was excluded from the study due to the lack of some segmentation results of the original cases. The correlation analysis between measured volumes and real volumes for each segmentation method before and after restoration is shown in Figure 4.2. provides the correlation analysis between measured volumes and ground truth volumes for five segmentation methods. As seen in this figure, all segmentation methods used yielded overestimated volumes compared to real volumes for all sizes of spheres before restoration, especially for small spheres due to the PVE. After the restoration process, these high-volume differences decreased in all segmentation methods for spheres less than 22 mm in size. However, only the FCM increased the volume differences for spheres larger than 20 mm in size.

Table 4.2 presents the range and the mean of the JI values obtained from the overlap measurement of segmented volumes of original and restored spherical lesions. For each segmentation technique, two-tailed paired sample t-test is used to analyze the relationship between two related groups, i.e. segmented original volumes versus ground truth volumes as well as segmented restored volumes versus ground truth volumes. The mean JI values of the restored images varied between 0.68 and 0.71 which are higher than those of the original segmented volumes. The further statistical test reveals that there are significant differences ($p<0.05$) between original segmented volumes and

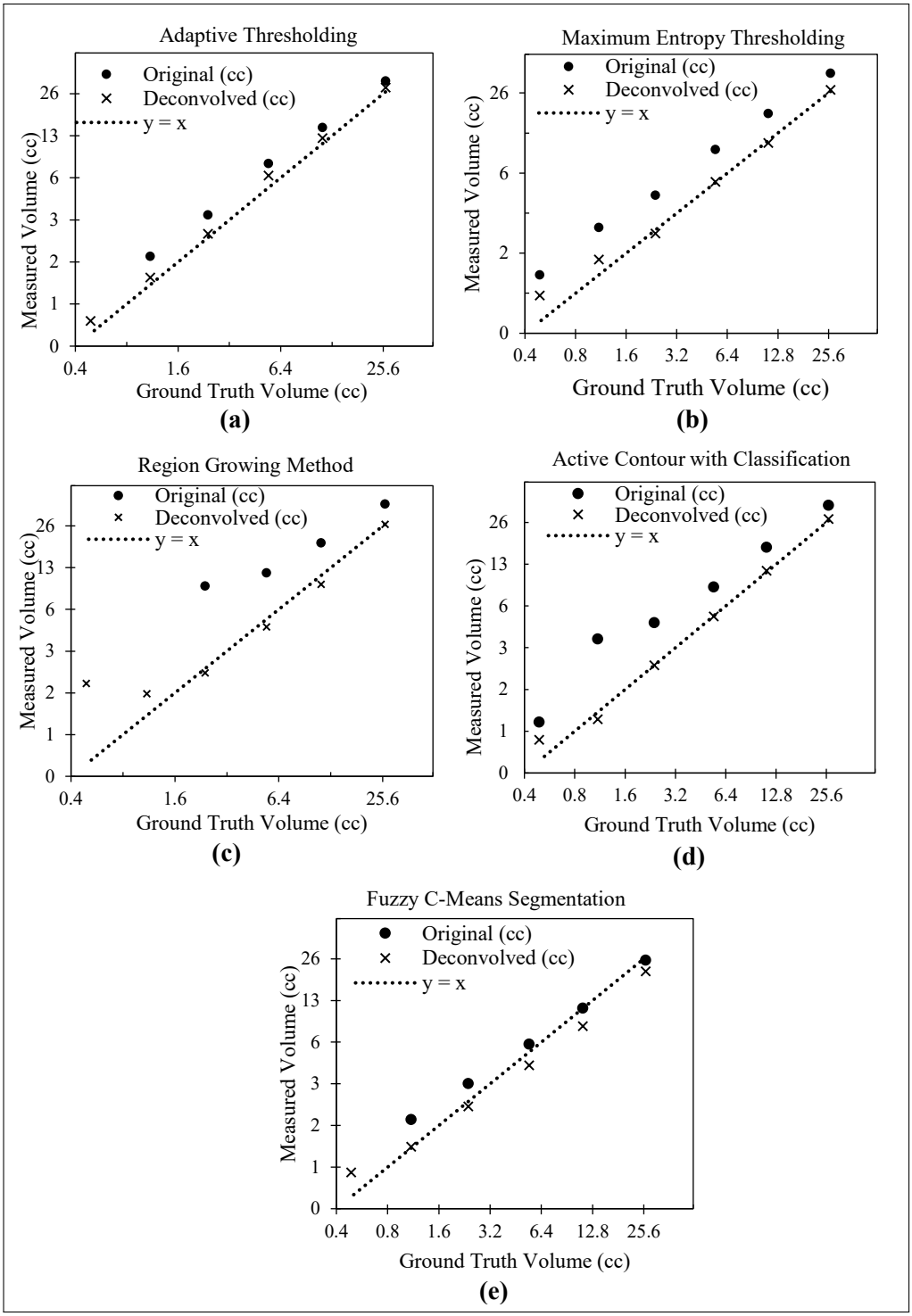

Figure 4.2 Comparisons of measured lesion volumes with ground truth volumes with respect to five segmentation methods (Dataset 1). Adaptive Thresholding in (a), Maximum Entropy Thresholding in (b), Region Growing in (c), Active Contour with Classification in (d), and Fuzzy C-Means Segmentation in (e). The dotted line shows where the measured volume and true volume are equal. These data belong to six spherical lesions with volumes ranging from 0.49 to 26.34 cc. Note that x and y-axes are plotted on a logarithmic scale with base 2.

reference volumes except the FCM. However, no significant differences ($p>0.05$) are found between restored segmented volumes and reference volumes for all segmentation techniques; that is, implementation of the local blind deconvolution on original PET lesions improves volume measurements and yields similar results with their true values.

Table 4.2
Overlap measurements (JI) in relation to real volumes of the spheres obtained from Dataset 1.

	JI in relation to Ground Truth			
Seg. Methods	**Range**	**Mean**	**SD**	**p value**
AT (Original)	0.57-0.78	0.65	0.08	<0.05
AT (Restored)	0.62-0.83	**0.70**	**0.08**	**0.06**
MET (Original)	0.42-0.70	0.56	0.10	<0.05
MET (Restored)	0.59-0.84	**0.70**	**0.10**	**0.57**
RG (Original)	0.27-0.69	0.50	0.18	<0.05
RG (Restored)	0.62-0.83	**0.71**	**0.09**	**0.33**
ACWC (Original)	0.50-0.74	0.59	0.10	<0.05
ACWC (Restored)	0.62-0.84	**0.71**	**0.09**	**0.36**
FCM (Original)	0.57-0.85	0.70	0.11	**0.69**
FCM (Restored)	0.63-0.80	**0.68**	**0.07**	**0.14**

Finally, to assess the effect of the restoration on foreground and background voxels, activity profiles of the lines passing from the center of the spheres were plotted on the central slice of the restored and original images as shown in Figure 4.3. There is a clear trend of increases in voxel intensities of foreground regions for all locally deconvolved lesions compared with original lesions. Nevertheless, no increase is observed in background regions.

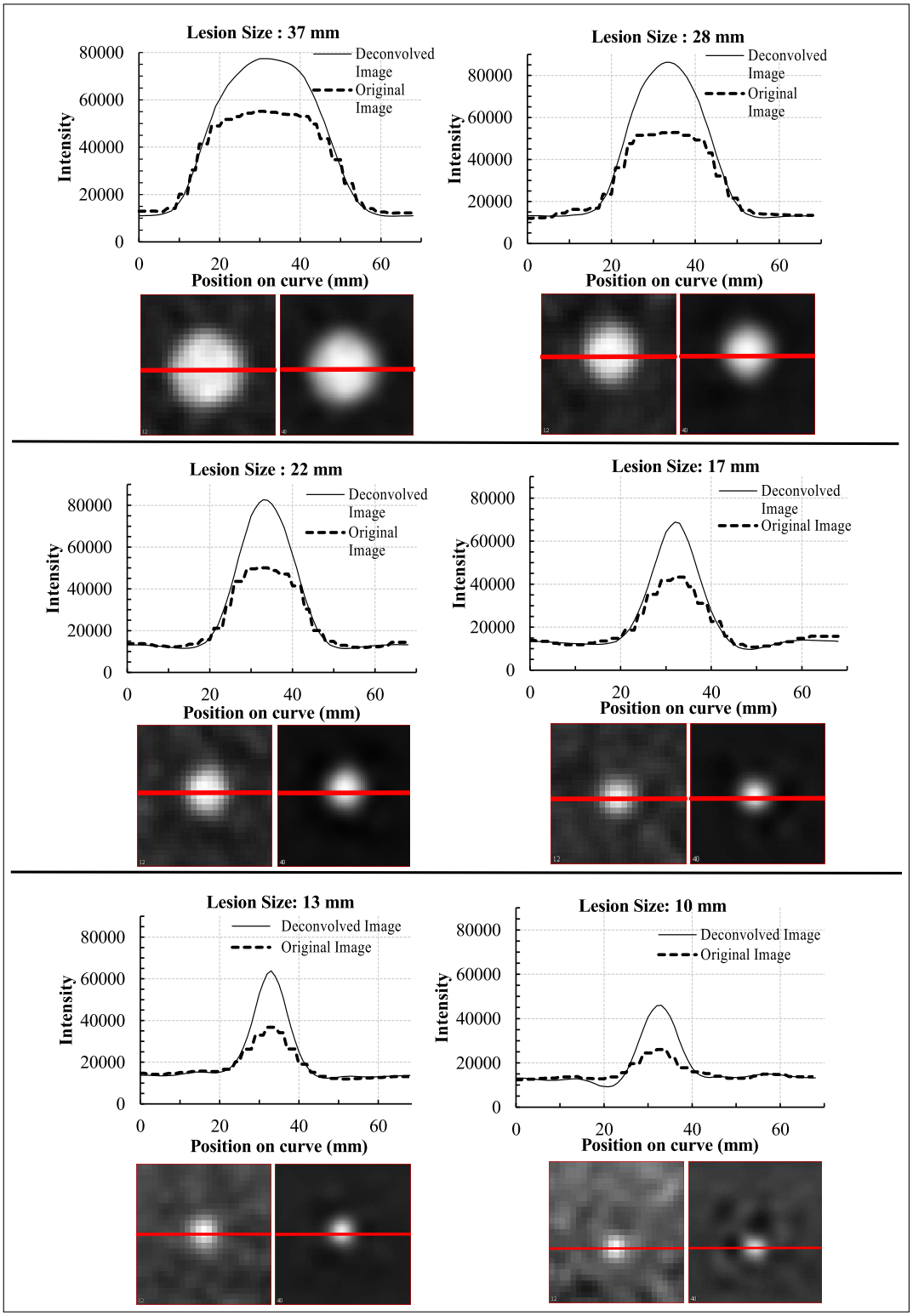

Figure 4.3 Intensity profiles of the original and restored phantom lesions at SBR of 4:1 (Dataset 1). Note that for each lesion, original and recovered images are displayed on the left side and on the right side, respectively.

4.2 Results of the Realistic Simulated Whole Body ^{18}F-FDG PET Oncology Images

The same methodological procedures are applied for simulated PET images as in phantom images. Volume measurement results of the PET image segmentation methods used with and without blind deconvolution method are presented in Table 4.3 and Figure 4.4. As seen from this table and figure, three methods (the MET, the RG, and the FCM) could not segment any lesion on original data. In addition, other methods (the AT and the ACWC) overestimated lesion volumes compared with ground truth volumes. However, all lesion volumes could be measured by each segmentation technique after implementation of the local blind deconvolution method.

The best volume estimation accuracy and precision were observed for the lesion size of 14 mm at SBR of 10 after deconvolution. The mean volume error percentage and SD of the five methods is 12.15%±8.27% for this lesion. When the SBR value decreases, the volume percentage error rates increase for all types of lesions. For instance, when the SBR value decreases from 10 to 4, the volume percentage error rate of the ACWC increases from 13.62% to 19.26% for the lesion size of 14 mm, and from 16.75% to 20.17% for the lesion sizes of 10.5 mm. Overall, for all lesion types with blind deconvolution, the ACWC is the most accurate and precise even in the worst case. The measured mean volume error percentage and SD of the recovered lesions is 17.45±2.94 (minimum: 13.62%, maximum:20.17%). The cause of this improvement is obvious from the intensity profiles of the original and restored lesions shown in Figure4.5. Line intensities of recovered lesion regions have been significantly increased compared with original images.

Table 4.3

Segmentation results and absolute percentage errors of the Dataset 2 with respect to various segmentation techniques for original and restored cases.

	Segmentation Methods										
Lesions	**AT**		**MET**		**RG**		**ACWC**		**FCM**		
(mm/SBR)	**Orig.(cc)**[7]	**Dec.(cc)**[8]	**Orig.(cc)**	**Dec.(cc)**	**Orig.(cc)**	**Dec.(cc)**	**Orig.(cc)**	**Dec.(cc)**	**Orig.(cc)**	**Dec.(cc)**	**G. Truth (cc)**[9]
14/10	4.16	1.54	-	1.83	-[10]	1.42	3.75	1.32	-	1.82	1.52
14/4	6.09	2.39	-	2.59	-	4.47	9.07	1.23	-	3.36	1.52
10.5/10	3.95	1.02	-	1.27	-	1.34	9.07	0.75	-	1.91	0.64
10.5/4	4.41	1.20	-	2.27	-	2.22	9.07	0.77	-	1.90	0.64
Mean±SD	4.66±0.98	**1.54±0.61**	**-**	**1.99±0.57**	**-**	**2.36±1.46**	7.74±2.66	**1.02±0.30**	-	**2.25±0.74**	**1.08±0.51**
Lesions	**Orig.(VE%)**[11]	**Dec.(VE%)**[12]	**Orig.(VE%)**	**Dec.(VE%)**	**Orig.(VE%)**	**Dec.(VE%)**	**Orig.(VE%)**	**Dec.(VE%)**	**Orig.(VE%)**	**Dec.(VE%)**	
14/10	173.10	0.74	-	20.22	-	7.00	146.02	13.62	-	19.17	
14/4	299.49	57.01	-	69.80	-	193.04	495.14	19.26	-	120.00	
10.5/10	544.09	58.42	-	97.44	-	107.70	1311	16.75	-	197.25	
10.5/4	586.07	85.94	-	252.44	-	245.13	1311	20.17	-	195.38	
Mean±SD	401±197	**51±36**	-	**101±100**	-	**138±104**	816±589	**17.45±2.94**	-	**133±84**	

[7]Orig.(cc) indicates the segmented volume of the original lesion.

[8]Dec.(cc) indicates the segmented volume of the restored lesion.

[9]The reference, ground truth volumes, of the lesions is denoted by G. Truth (cc).

[10]The lesion could not be segmented with the specified method.

[11]Orig.(VE%) denotes the percentage volume error of the simulated PET lesion and calculated using Eq. 2.2.

[12]Dec.(VE%) denotes the percentage volume error of the restored simulated PET lesion and calculated using Eq. 2.2.

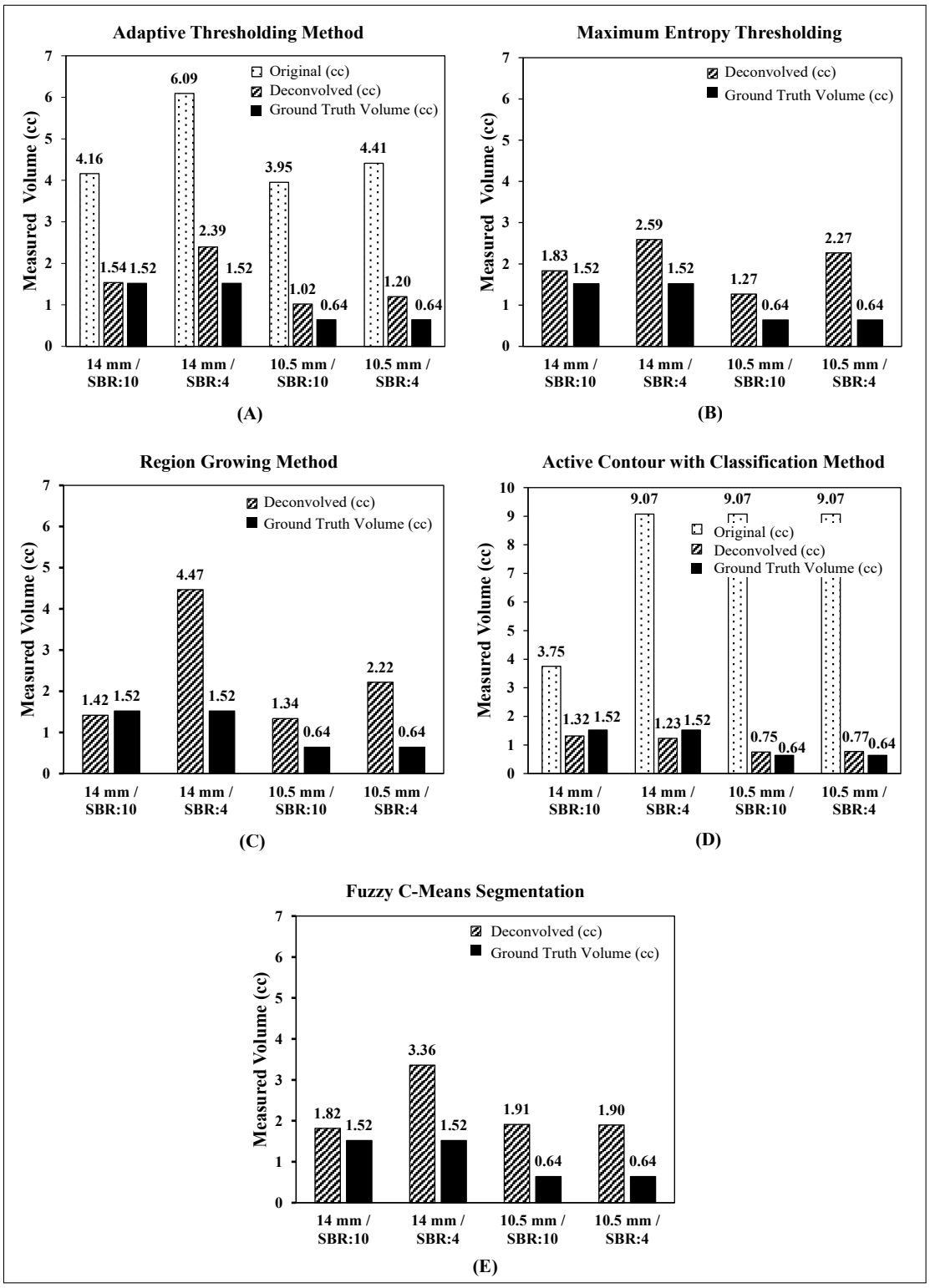

Figure 4.4 Measured lesion volumes using various PET image segmentation methods with and without blind deconvolution for Dataset 2.

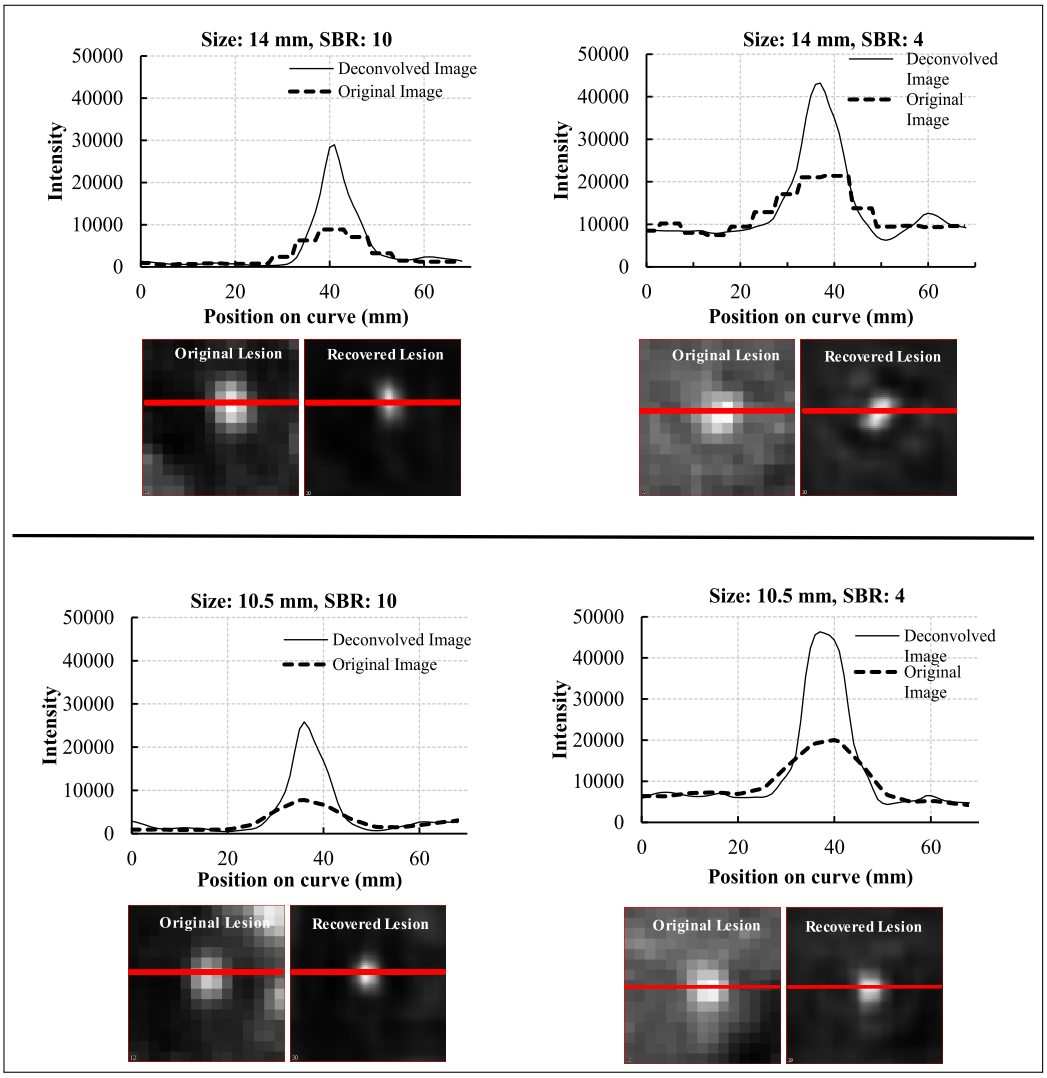

Figure 4.5 Intensity profiles of the original and restored simulated PET Oncology images (Dataset 2).

4.3 Results of the The Clinically Relevant Large Tumors

The last source of data includes six patient images which have clinically resembled large lesions with arbitrary shapes and heterogeneous activity distributions. The same restoration steps are implemented on these lesions as in the first two datasets. The results of the segmentation analysis before and after restoration are presented in Table 4.4. As seen from this table, for original lesions, each segmentation technique yields a lower mean volume estimation error (minimum: 7.67%, maximum: 32.61%) than the result of the other datasets. Minimum mean error rate (7.67%±6.08%) is calculated with the MET for these original large lesions.

Table 4.4

Segmentation results and absolute percentage errors of the Dataset 3 with respect to various segmentation techniques for original and restored cases.

	Segmentation Methods										
	AT		**MET**		**RG**		**ACWC**		**FCM**		
Lesions	**Orig.(cc)**[13]	**Dec.(cc)**[14]	**Orig.(cc)**	**Dec.(cc)**	**Orig.(cc)**	**Dec.(cc)**	**Orig.(cc)**	**Dec.(cc)**	**Orig.(cc)**	**Dec.(cc)**	**G. Truth (cc)**[15]
Patient 1	40.32	34.49	35.65	31.57	46.34	36.22	60.42	39.16	32.51	26.64	40.38
Patient 2	208.51	189.05	200.90	172.52	296.00	276.10	239.10	180.85	167.81	145.50	203.84
Patient 3	84.03	65.70	64.32	44.06	82.82	61.16	97.22	56.20	71.94	49.46	65.60
Patient 4	176.26	158.42	162.82	139.77	229.12	248.80	224.64	186.10	150.59	130.71	196.35
Patient 5	61.12	48.24	51.20	33.41	78.46	50.22	77.06	51.77	48.83	32.69	53.89
Patient 6	64.38	53.27	52.10	35.31	66.37	51.12	70.40	58.89	49.60	35.09	57.15
Lesions	**Orig.(VE%)**[16]	**Dec.(VE%)**[17]	**Orig.(VE%)**	**Dec.(VE%)**	**Orig.(VE%)**	**Dec.(VE%)**	**Orig.(VE%)**	**Dec.(VE%)**	**Orig.(VE%)**	**Dec.(VE%)**	
Patient 1	0.16	14.61	11.73	21.83	14.74	10.30	49.60	3.02	19.49	34.02	
Patient 2	2.29	7.26	1.44	15.37	45.21	35.45	17.30	11.28	17.68	28.62	
Patient 3	28.09	0.14	1.95	32.84	26.24	6.76	48.20	14.33	9.66	24.61	
Patient 4	10.23	19.32	17.08	28.82	16.69	26.71	14.41	5.22	23.31	33.43	
Patient 5	13.42	10.49	4.99	38.00	45.61	6.80	42.99	3.92	9.38	39.34	
Patient 6	12.65	6.80	8.85	38.22	16.13	10.56	23.18	3.04	13.21	38.60	
Mean±SD	11.14±9.95	**9.77±6.68**	7.67±6.08	**29.18±9.14**	27.44±14.51	**16.10±12.04**	32.61±16.09	**6.80±4.81**	15.45±5.63	**33.10±5.70**	

[13]The segmented volume of the original lesion is denoted by Orig.(cc).

[14]The segmented volume of the restored lesion is denoted by Dec.(cc).

[15]The reference, ground truth volume, of the lesions is denoted by G. Truth (cc).

[16]Orig.(VE%) denotes the percentage volume error of the lesion and calculated using Eq. 2.2.

[17]Dec.(VE%) denotes the percentage volume error of the restored lesion and calculated using Eq. 2.2.

After the restoration process, the mean volume percentage errors decrease from 11.14% to 9.77% for the AT, from 27.44% to 16.10% for the RG, and from 32.61% to 6.80% for the ACWC. Nevertheless, the mean percentage errors of the lesion volumes tend to increase from 7.67% to 29.18% for the MET, and from 15.45% to 33.10% for the FCM method. As in the previous datasets, for recovered lesions, the ACWC is more accurate and precise (6.80±4.81) among the segmentation methods used.

Table 4.5 shows the overlap measurements of the segmented lesion volumes before and after the restoration process. Mean JI values increase for two segmentation methods (the ACWC and the RG) with restoration. Efficiency of each segmentation technique is evaluated using two-tailed paired sample t-test for two paired groups (original versus ground truth and restored versus ground truth). The statistical test reveals that there are no significant differences ($p>0.05$) between original segmented volumes and reference volumes except the ACWC. That is, large lesion volumes can be measured close to the ground truth volumes with most of the PET segmentation methods without any processing. However, when the blind deconvolution is implemented on these large lesions, the ACWC is the best choice thanks to its high accuracy and precision (Mean Error%±SD%: 6.80%±4.81% and Mean JI±SD: 0.78±0.05).

Table 4.5
Overlap measurements (JI) in relation to real volumes of the spheres obtained from Dataset 3.

	JI in relation to Ground Truth			
Seg. Methods	**Range**	**Mean**	**SD**	**p value**
AT (Original)	0.65-0.85	0.76	0.06	0.603
AT (Restored)	0.71-0.79	0.75	0.03	0.102
MET (Original)	0.71-0.82	0.78	0.04	0.159
MET (Restored)	0.60-0.74	0.67	0.07	**<0.05**
RG (Original)	0.62-0.81	0.72	0.09	0.067
RG (Restored)	0.65-0.79	**0.73**	**0.06**	0.271
ACWC (Original)	0.55-0.83	0.70	0.09	**<0.05**
ACWC (Restored)	0.70-0.83	**0.78**	**0.05**	0.101
FCM (Original)	0.70-0.82	0.77	0.04	0.110
FCM (Restored)	0.60-0.70	0.65	0.04	**<0.05**

The intensity values of the line profiles in lesion regions have been compared

for original and recovered images as shown in Figure 4.6. When we compared the intensity profiles of the three datasets (Figure 4.3, Figure 4.5, and Figure 4.6), we observed less intensity increase with the blind deconvolution in large lesions compared to small lesions. The most probable cause of this difference is associated with the number of iterations used in the deconvolution. Table 3.6 shows that the CNR values of the large lesions reach a maximum with fewer numbers of iterations. This fact may be a result of the PVE's limited effect on large lesions.

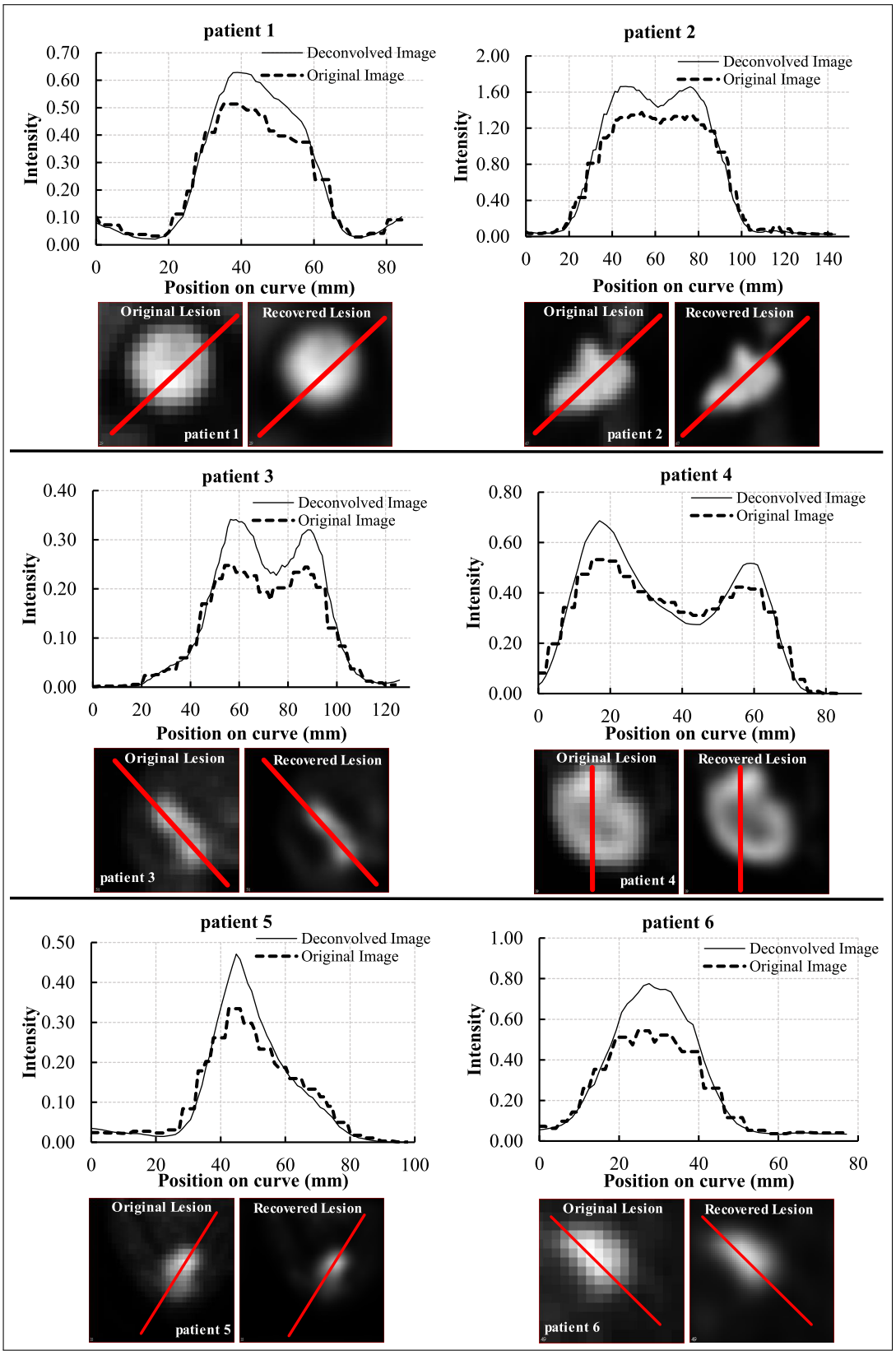

Figure 4.6 Intensity profiles of the original and restored clinically relevant patient images (Dataset 3).

5. DISCUSSION

As we have seen from literature studies in section 2.1, numerous factors could affect the accuracy of segmentation methods, i.e. scanner or image resolution, scanner type and settings of image reconstruction algorithms, image filtering, level of image noise, and tumor characteristics. Therefore, accurate segmentation of lesions from the PET/CT image has vital importance in terms of treatment planning, as far as its position, shape, and volume are concerned. The initial objective of this study was to determine the optimal segmentation methodology using local blind deconvolution and resampling to accurately and precisely measure metabolically active PET lesion volumes.

PET image segmentation studies from Table 2.1 have shown that each segmentation technique has a different measurement error, and the best segmentation methods have less than 10 percent. For instance, in a study of Hatt et al. [17], the Fuzzy Locally Adaptive Bayesian (FLAB) segmentation method showed superior performance compared to the thresholding, the FCM, and the Fuzzy Hidden Markov Chain (FHMC) methods; while Firouzian et al. [25] found that the contrast-oriented thresholding and the AT methods have provided better results for phantom lesions and irregular shapes of lesions respectively, compared to the fixed thresholding and the FLAB methods. Thus, there is no consensus among researchers on a single segmentation method apt for varying patient, image acquisition, and reconstruction parameters.

5.1 Main Findings

In our study, various segmentation methods were compared with respect to the patient parameters (lesion size and shape, SBR, uptake heterogeneity) and the restoration method used. The chart summarizing the performance of the segmentation methods on phantom lesions is presented in Figure 5.1, and all measurement errors

are analyzed in terms of lesion size and the PVC method. When we compare the performance of segmentation methods in terms of restoration, for all phantom spheres, the CNR-guided ROI-based deconvolution significantly reduces volume estimation errors (minimum error: 3.37%±4.49% [ACWC method], maximum error: 15.59%±9.98% [FCM method]). For small lesions (<22 mm), the restoration improves accuracy and precision of all segmentation methods (minimum errors: 5.22%±4.69% [FCM method] and 5.61%±7.88% [ACWC method], maximum error: 25.10%±25.96% [RG method]). For larger lesions (sized 22-37 mm), volume errors of all segmentation techniques used except the FCM decrease with blind deconvolution method (minimum error: 1.88% ± 1.01% [ACWC method], maximum error: 22.50% ± 3.04% [FCM method]).

If the radiologist needs to measure volumes of small lesions which resemble spheroids with homogeneous activity distributions, the ACWC, the FCM, and the AT methods will be best practical options with the proposed restoration method (volume error <10%). For larger lesions, all techniques without the FCM method will be preferable choices. Thus, these findings and methods will be an important contribution to the development of the first segmentation flow map that will benefit PET specialists for accurate and precise volume measurements of various lesions.

In the second data set, the effect of the SBR is investigated with respect to the restoration. Images of this dataset consisted of large pixel sizes (5.06 mm) and small spherical lesions with 10.5 mm and 14 mm in diameter. Normally, a lesion of 10.5 mm in diameter cannot be represented by 2 large pixels. Therefore, the PVE results from large pixel sizes in small lesions in the image. In this worst case, none of the segmentation techniques are capable to segment these small lesions accurately without restoration. However, after the restoration process, all techniques provide useful results for lesions sized 14 mm in diameter and SBR of 10 (min: 0.74%, max: 20.22%). When SBR decreases from 10 to 4, bias increases for all segmentation techniques, consistent with the findings of Cheebsumon et al. [4]. For all lesions included in the second dataset, the ACWC seems to be the best method on average (17.45±2.94).

Furthermore, the execution time of the local restoration method is a signifi-

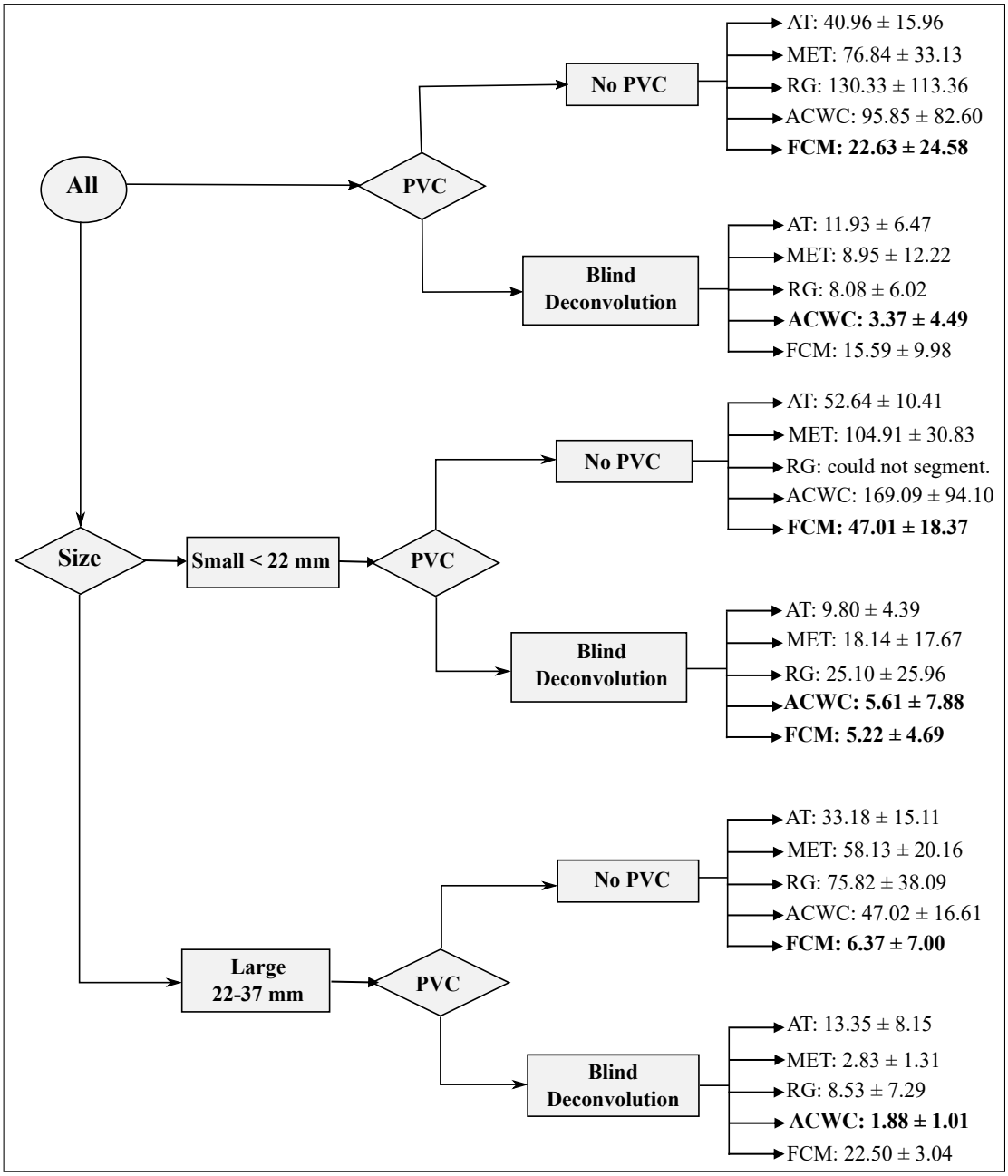

Figure 5.1 The chart that summarizes the performance of the segmentation methods on phantom lesions in terms of VE%. Note that AT is the Adaptive Thresholding, MET is the Maximum Entropy Thresholding, RG is the Region Growing, ACWC is the Active Contour with Classification, and FCM is the Fuzzy C-Means segmentation methods.

cant variable in terms of computational cost, as far as its positive impact on accurate segmentation is concerned. Therefore, the efficiency of the local restoration method is compared with the whole image deconvolution regarding the computation time of the algorithms on the second dataset. For the local restoration, the best values of the parameters (the initial PSF kernels and the iteration values) were selected from Table 3.5 for each lesion. For the whole image restoration, the initial PSF kernel of 4x4x4 voxels was used with iteration values acquired from Table 3.5. Each algorithm was implemented using MATLAB 2015a on a dual-core 2.53 GHz Intel Core i5 CPU. As shown in Table 5.1, the CPU time is significantly reduced in average ∼13-fold with respect to deconvolving the entire image volume using the local extraction method [48].

Table 5.1
The comparison of the execution times of the local blind deconvolution and the whole image blind deconvolution (obtained from the reference [48]).

Lesions (mm/SBR)	**The best iteration number**	**CPU Time of the whole image deconvolution (sec)**	**CPU time of the local deconvolution (sec)**
14/10	15	89.2	8
14/4	15	89.6	6.6
10.5/10	15	89.6	6.4
10.5/4	20	101.5	6.5
Mean		92.48	6.88

In the third data set large lesions with arbitrary shapes and heterogeneous activity distributions are restored, and lesion volumes are measured before and after the restoration process. We have seen that volume errors of the third dataset are lower than others. This is an expected result because intrinsic and extrinsic factors cause less degradation in image quality on large lesions. After the restoration process, significant deterioration is observed on volume estimation accuracy for two segmentation algorithms (the MET and the FCM). It should be noted that the FCM method was implemented on the restored images with an improved CNR. Despite this, the fact that the segmentation resulted in an increased error maybe explained by the inability of this method to function well with real lesions.

In addition, no statistically significant difference was found between two groups

(original v. true and restored v. true) in terms of segmentation accuracy for the AT and the RG methods. However, for the ACWC, significant improvements were observed. All segmentation techniques except the ACWC were capable to segment these lesions without restoration. This is consistent with findings of past studies by Soret et al. [5] and Hatt et al. [41] who conclude that the PVE depends on the size of the lesion, and large lesions are less affected by the PVE. As a result, if the radiologist prefers to use our proposed method on large lesions (mean volume: 102.87 cc, ranging from 40.38 cc to 203.84 cc), the ACWC may be a good option based on these experiments. Furthermore, as stated above, not all automatic segmentation algorithms are able to delineate realistic heterogeneous tumors correctly; however, Table 3.5 shows that CNR is systematically better for all tumors after deconvolution. Therefore, it would be useful to verify automatic delineation results visually and after deconvolution.

5.2 Comparison with Literature

This study differs from previous work in that the CNR and ROI-based deconvolution was used together with resampling. The image is first restored before automatic segmentation. Figure 5.2(a) shows the advantage of using CNR and ROI based deconvolution. It can be seen that deconvolution improves CNR. The best iteration number should be selected based on Figure 5.2.

Most iteration control methods use metrics such as Mean Square Error (MSE), Mean Absolute Error (MAE), and Signal to Noise Ratio (SNR) [71]. These methods make the iterative algorithm stop with respect to a criterion and a threshold when there is no further advantage. However, these methods are not designed for predicting the iteration number that yields the least segmentation error on an image. As can be seen in Figure 5.2(b), Figure 5.2(c), and Figure 5.2(d), CNR yields a peak, helping us to find the approximate iteration number for the best recovered image [63]. Note that the right iteration number can be found by sequentially computing the CNR either starting from the value of 1 for a given tumor (preferably in an automated fashion) or by estimating an initial iteration number for starting the search by consulting CNR

versus iteration results obtained from previous experiments. Note that this can be expanded continuously by including the results of new tumor delineation cases.

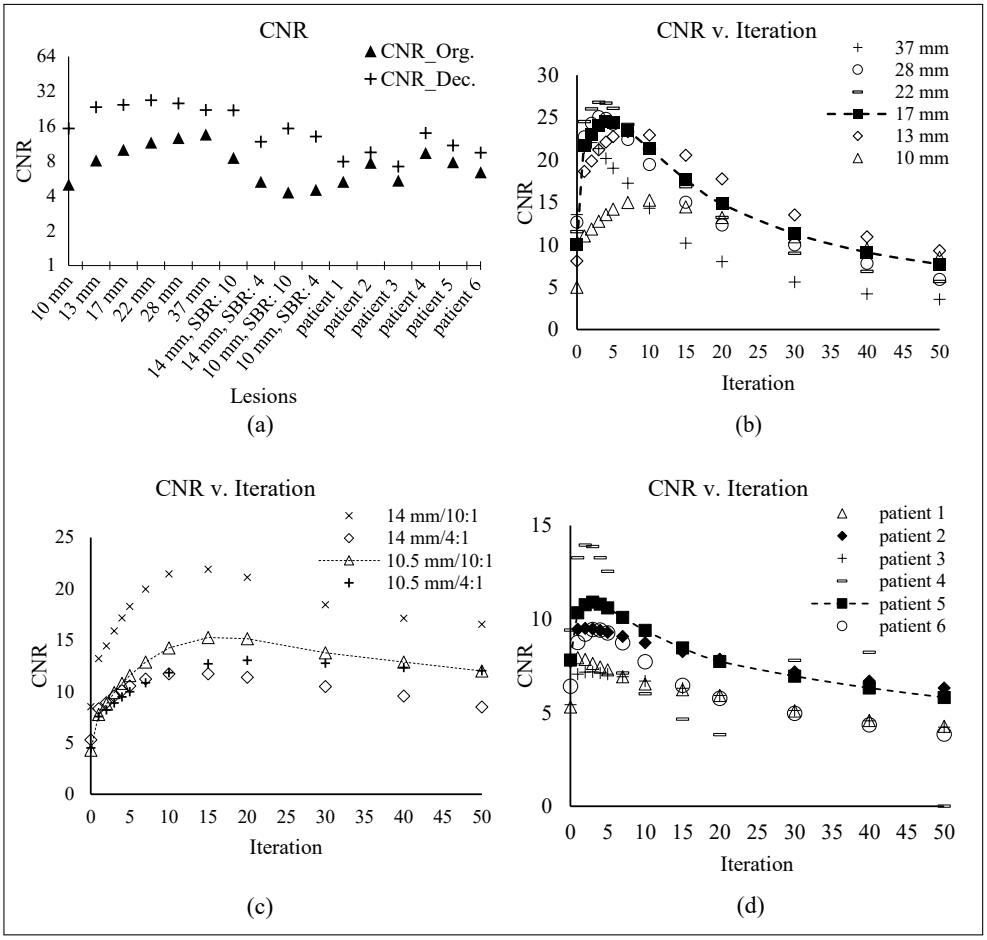

Figure 5.2 CNR values for all lesions before and after restoration (a), CNR values with respect to iterations are shown in (b) for the dataset 1, in (c) for the dataset 2, and in (d) for the Dataset 3.

The local deconvolution of the reconstructed image resulted in several advantages over the deconvolution of the whole 3D image as expressed in the above sections. First, the PSF could be taken fixed for a small region. Second, the execution time was significantly reduced. Third, deconvolution can be performed for any residual PVE that can remain after reconstruction for a particular tumor region. Finally, this method does not suffer from PSF prediction errors during reconstruction. Therefore, by using both CNR- and ROI-based deconvolution, it was possible to significantly increase delineation accuracy while reducing computational time and implementation complexity as described in the text.

Taking these advantages into account, it would be useful to compare this restoration method with other methods, if data sets and other conditions are the same. On the other hand, in case of different conditions, Table 5.2 compares our method with the state-of-the-art studies in terms of the volume estimation error and the computation time. Xu et al. (2018) proposed a joint solution for post-reconstruction PET images by utilizing interactions among segmentation, denoising, and PVC processes [72]. They used the NEMA NU-2 IQ Phantom containing six spheres with sizes ranging from 10 to 37 mm, clinical and pre-clinical PET. They measured the average segmentation error for only phantom data and found the DSC of 0.9275. This average error rate is better than ours. However, it should be noted that the metric of DSC yields better results compared to the JI. In addition, their average processing time is 5 seconds per slice and about 5 minutes are needed to implement their proposed method. This computational time is higher than ours.

In another study, Li et al. applied integrated total variation semi-blind deconvolution and Mumford-Shah segmentation with multiple regularization methods on phantom and clinical data [47]. Their phantom and other imaging parameters were different from our input parameters. Similarly, small volumes ranging from 0.5 to 20 mL were measured using several segmentation methods at SBR values of 2, 4, 8, and 16. Despite these higher SBR values, they found the VE% of 20%, the CE of 41%, and the DSI of 0.77 for averaged over all sphere sizes and SBRs of the phantom. When these results are compared with our findings, on the one hand, our segmentation accuracy (the VE%: 3.37%) is superior to theirs. On the other hand, their overlap measurement (DSI: 0.77) is slightly better than our finding (JI: 0.71). This difference is the result of the use of two different metrics such as DSI and JI. As stated in the previous paragraph, the metric of DSC yields better results compared to the JI. This was the one of the limitations of our study. Finally, the execution time of their method was several minutes for one patient. However, high computational costs may be induced if there are more optimal solutions than one for the regularization step.

Table 5.2
Comparison of the state-of-the-art studies with our method.

Related Works	Segmentation and PVC Methods	Data Types	Volume Measurement Error	Computation Time
Xu et al. (2018) [72]	Volume Consistency-Based Iterative Voxel-Based Correction Algorithm for PVC, Generalized Anscombe Transformation for denoising, and Affinity Propagation Based Iterative Clustering Method for segmentation	Phantom, clinical, and pre-clinical PET scans	With the use of denoising and PVC steps, they measured 7.25% (DSC[1]: 92.75%) average segmentation error for the Nema phantom spheres. Without denoising and PVC steps, the resulting average error was found 25.3% (DSC: 74.7%).	The average processing time was 5 s per slice.
Li et al. (2017) [47]	Integrated total variation semi-blind deconvolution with multiple regularization (for PVC). Mumford-Shah segmentation, 40% thresholding, 50% thresholding, Otsu thresholding, Active contour, Geodesic active contour, FCM, and Graph cuts methods (for segmentation).	Phantom and clinical data	Their method performed better results compared to other segmentation methods in terms of DSI[2] (0.77), CE[3] (41%), and VE[4] (20%) for averaged over all sphere sizes and SBRs of the phantom data.	The typical computation time was about several minutes for one patient.
Our Method	Local blind deconvolution and resampling (for PVC). Adaptive Thresholding (42% and 50%), Maximum Entropy Thresholding, Region Growing, Active Contour with Classification, and FCM (for segmentation).	Phantom and simulated clinical images	With the use of the active contour with classification technique, the mean VE was reduced to 3.37% and the mean JI[5] value was found 0.71 for all lesions of the phantom dataset.	The typical computation time was less than a minute for a 3-D image of the lesion.

5.3 Limitations and Future Work

The scope of this study was limited in terms of segmentation algorithms, datasets, and PET scanners. Despite the five kinds of segmentation algorithms used, we did not apply all PET segmentation methods and manual delineation.

[1]DSC: Dice Similarity Coefficient
[2]DSI: Dice Similarity Index
[3]CE: Classification Error
[4]VE: Volume Error Percentage
[5]JI: Jaccard Index

6. CONCLUSION

Accurate tumor volume measurement has been a controversial and much disputed subject within the field of the PET imaging. We improved the accuracy of the various PET segmentation methods for volume quantification on PET images combining two methods: the local blind deconvolution and resampling. The goal in this work is to study the impact of blind deconvolution and processing parameters on the accuracy of automated delineation algorithms and then to optimize the accuracy with respect to these parameters. The method was tested on tumors of different sizes and SBR conditions successfully. Therefore, the primary motivation is fundamentally to help guide medical professionals in making better delineation that will ultimately benefit their patients.

In conclusion, the method described in this study can significantly reduce tumor delineation errors. It can be practically used by combining the best automatic segmentation routine with resampling and a modified deconvolution scheme based on the blind restoration method. The procedure should take a few minutes, not needing a special software. Future work is needed to automate these procedures.

6.1 List of publications produced from the thesis

1. "Optimising delineation accuracy of tumours in pet for radiotherapy planning using blind deconvolution," Guvenis, A. and Koc, A., *Radiation Protection Dosimetry*, Vol. 165, no. 1-4, pp. 495-498, 2015.

2. "3-D Tumor Delineation in Positron Emission Tomography reconstructed images restored by the use of Lucy Richardson blind deconvolution method," Koc, A. and Guvenis, A., *in IUPESM 2015 World Congress on Medical Physics and Biomedical Engineering*, Abstract Book, pp. 527, 2015.

3. "Implementation method in blind deconvolution based tumor segmentation using

simulated pet images," Koc, A. and Guvenis, A., *in Medical Technologies National Congress (TIPTEKNO), 2017*, pp. 1-4, IEEE, 2017.

4. "Design and evaluation of an accurate CNR-guided small region iterative restoration-based tumor segmentation scheme for PET using both simulated and real heterogeneous tumors," Koc, A. and Guvenis, A., *Submitted to the Journal of Medical & Biological Engineering & Computing*, 2019

APPENDIX A. BLIND DECONVOLUTION ALGORITHM

I = load_untouch_nii('input_image.nii');

This function loads locally cropped image into I.

A = double (I.img (:,:,:));

Image types (16 bit and 32 bit) are converted to type double.

3D_Kernel = ones(x,y,z);

This array is the edgetaper kernel obtained from the background region. Each number indicates the distance in voxels from the border of the image to the nearest lesion region measured by visual inspection for each image cropped locally. Table A.1 presents the kernel sizes used in the edgetaper function.

Table A.1
Edgetaper kernel sizes used to reduce ringing artifacts for various lesion sizes.

	Lesions	Kernel Sizes in Voxels
Dataset 1	**37 mm**	10x10x15
	28 mm	18x18x25
	22 mm	20x20x30
	17 mm	20x20x30
	13 mm	25x25x30
	10 mm	25x21x30
Dataset 2	**14 mm, SBR: 10**	27x18x18
	14 mm, SBR: 4	30x26x23
	10 mm, SBR: 10	27x23x20
	10 mm, SBR: 4	30x30x25
Dataset 3	**patient 1**	12x9x4
	patient 2	10x15x11
	patient 3	17x16x6
	patient 4	13x6x3
	patient 5	26x16x4
	patient 6	10x8x4

INITPSF = ones(x,y,z);

INITPSF, one of the parameters of the deconvolution process, represents the PSF kernel size to be used in deconvolution. Due to the spatial distortion in the recon-

structed PET images, four separate PSF kernel sizes (13x13x13, 15x15x15, 17x17x17, and 21x21x21) were used for the deconvolution process. After the restoration process, the best PSF kernel size was determined using the CNR for each lesion.

B = edgetaper(A,3D_Kernel);

This function blurs the edges of image A using 3D_Kernel, and reduces the ringing artifacts in blind deconvolution. Image B, which is the output of this function, is then used as the input of the blind deconvolution.

[J, P] = deconvblind(B, INITPSF, ITERATION);

The deconvblind function deconvolves image B using two additional parameters (INITPSF and ITERATION). It returns both deconvolved image J and restored PSF P in each iteration. The loop continues until the number of iterations used (1, 2, 3, 4, 5, 7, 10, 15, 20, 30, 40, and 50). In total, 16 outputs (J and P) are generated for each lesion, 4 for the INITPSF and 12 for the ITERATION. The best INITPSF and ITERATION values are then calculated using CNR.

debimg(:,:,:)=J;

I.img=debimg;

save_untouch_nii(I,'Restored_image');

save_untouch_nii(I,'Restored_PSF');

REFERENCES

1. Emre Erdi, Y., "The use of pet for radiotherapy," *Current Medical Imaging Reviews*, Vol. 3, no. 1, pp. 3–16, 2007.

2. Terasawa, T., T. Dvorak, S. Ip, G. Raman, J. Lau, and T. A. Trikalinos, "Systematic review: charged-particle radiation therapy for cancer," *Annals of Internal Medicine*, Vol. 151, no. 8, pp. 556–565, 2009.

3. Pan, T., and O. Mawlawi, "Pet/ct in radiation oncology," *Medical Physics*, Vol. 35, no. 11, pp. 4955–4966, 2008.

4. Cheebsumon, P., M. Yaqub, F. H. van Velden, O. S. Hoekstra, A. A. Lammertsma, and R. Boellaard, "Impact of [18f] fdg pet imaging parameters on automatic tumour delineation: need for improved tumour delineation methodology," *European Journal of Nuclear Medicine and Molecular Imaging*, Vol. 38, no. 12, pp. 2136–2144, 2011.

5. Soret, M., S. L. Bacharach, and I. Buvat, "Partial-volume effect in pet tumor imaging," *Journal of Nuclear Medicine*, Vol. 48, no. 6, pp. 932–945, 2007.

6. Foster, B., U. Bagci, A. Mansoor, Z. Xu, and D. J. Mollura, "A review on segmentation of positron emission tomography images," *Computers in Biology and Medicine*, Vol. 50, pp. 76–96, 2014.

7. Zaidi, H., and I. El Naqa, "Pet-guided delineation of radiation therapy treatment volumes: a survey of image segmentation techniques," *European Journal of Nuclear Medicine and Molecular Imaging*, Vol. 37, no. 11, pp. 2165–2187, 2010.

8. Boellaard, R., N. C. Krak, O. S. Hoekstra, and A. A. Lammertsma, "Effects of noise, image resolution, and roi definition on the accuracy of standard uptake values: a simulation study," *Journal of Nuclear Medicine*, Vol. 45, no. 9, pp. 1519–1527, 2004.

9. Schaefer, A., S. Kremp, D. Hellwig, C. Rübe, C.-M. Kirsch, and U. Nestle, "A contrast-oriented algorithm for fdg-pet-based delineation of tumour volumes for the radiotherapy of lung cancer: derivation from phantom measurements and validation in patient data," *European Journal of Nuclear Medicine and Molecular Imaging*, Vol. 35, no. 11, pp. 1989–1999, 2008.

10. van Dalen, J. A., A. L. Hoffmann, V. Dicken, W. V. Vogel, B. Wiering, T. J. Ruers, N. Karssemeijer, and W. J. Oyen, "A novel iterative method for lesion delineation and volumetric quantification with fdg pet," *Nuclear Medicine Communications*, Vol. 28, no. 6, pp. 485–493, 2007.

11. Daisne, J.-F., M. Sibomana, A. Bol, T. Doumont, M. Lonneux, and V. Grégoire, "Tri-dimensional automatic segmentation of pet volumes based on measured source-to-background ratios: influence of reconstruction algorithms," *Radiotherapy and Oncology*, Vol. 69, no. 3, pp. 247–250, 2003.

12. Nestle, U., S. Kremp, A. Schaefer-Schuler, C. Sebastian-Welsch, D. Hellwig, C. Rübe, and C.-M. Kirsch, "Comparison of different methods for delineation of 18f-fdg pet–positive tissue for target volume definition in radiotherapy of patients with non–small cell lung cancer," *Journal of Nuclear Medicine*, Vol. 46, no. 8, pp. 1342–1348, 2005.

13. Black, Q. C., I. S. Grills, L. L. Kestin, C.-Y. O. Wong, J. W. Wong, A. A. Martinez, and D. Yan, "Defining a radiotherapy target with positron emission tomography," *International Journal of Radiation Oncology* Biology* Physics*, Vol. 60, no. 4, pp. 1272–1282, 2004.

14. Biehl, K. J., F.-M. Kong, F. Dehdashti, J.-Y. Jin, S. Mutic, I. El Naqa, B. A. Siegel, and J. D. Bradley, "18f-fdg pet definition of gross tumor volume for radiotherapy of non–small cell lung cancer: Is a single standardized uptake value threshold approach appropriate?," *Journal of Nuclear Medicine*, Vol. 47, no. 11, pp. 1808–1812, 2006.

15. Jentzen, W., L. Freudenberg, E. G. Eising, M. Heinze, W. Brandau, and A. Bockisch, "Segmentation of pet volumes by iterative image thresholding," *Journal of Nuclear Medicine*, Vol. 48, no. 1, pp. 108–114, 2007.

16. Geets, X., J. A. Lee, A. Bol, M. Lonneux, and V. Grégoire, "A gradient-based method for segmenting fdg-pet images: methodology and validation," *European Journal of Nuclear Medicine and Molecular Imaging*, Vol. 34, no. 9, pp. 1427–1438, 2007.

17. Hatt, M., C. C. Le Rest, A. Turzo, C. Roux, and D. Visvikis, "A fuzzy locally adaptive bayesian segmentation approach for volume determination in pet," *IEEE Transactions on Medical Imaging*, Vol. 28, no. 6, pp. 881–893, 2009.

18. Hatt, M., C. C. Le Rest, P. Descourt, A. Dekker, D. De Ruysscher, M. Oellers, P. Lambin, O. Pradier, and D. Visvikis, "Accurate automatic delineation of heterogeneous functional volumes in positron emission tomography for oncology applications," *International Journal of Radiation Oncology* Biology* Physics*, Vol. 77, no. 1, pp. 301–308, 2010.

19. Hatt, M., C. C. Le Rest, N. Albarghach, O. Pradier, and D. Visvikis, "Pet functional volume delineation: a robustness and repeatability study," *European Journal of Nuclear Medicine and Molecular Imaging*, Vol. 38, no. 4, pp. 663–672, 2011.

20. Dewalle-Vignion, A.-S., N. Betrouni, R. Lopes, D. Huglo, S. Stute, and M. Vermandel, "A new method for volume segmentation of pet images, based on possibility theory," *IEEE Transactions on Medical Imaging*, Vol. 30, no. 2, pp. 409–423, 2011.

21. Khamwan, K., A. Krisanachinda, and C. Pluempitiwiriyawej, "Automated tumour boundary delineation on 18f-fdg pet images using active contour coupled with shifted-optimal thresholding method," *Physics in Medicine and Biology*, Vol. 57, no. 19, p. 5995, 2012.

22. Prieto, E., P. Lecumberri, M. Pagola, M. Gomez, I. Bilbao, M. Ecay, I. Penuelas, and J. M. Marti-Climent, "Twelve automated thresholding methods for segmentation of pet images: a phantom study," *Physics in Medicine and Biology*, Vol. 57, no. 12, p. 3963, 2012.

23. Zaidi, H., M. Abdoli, C. L. Fuentes, and I. M. El Naqa, "Comparative methods for pet image segmentation in pharyngolaryngeal squamous cell carcinoma," *European Journal of Nuclear Medicine and Molecular Imaging*, Vol. 39, no. 5, pp. 881–891, 2012.

24. Onoma, D., S. Ruan, S. Thureau, L. Nkhali, R. Modzelewski, G. Monnehan, P. Vera, and I. Gardin, "Segmentation of heterogeneous or small fdg pet positive tissue based on a 3d-locally adaptive random walk algorithm," *Computerized Medical Imaging and Graphics*, Vol. 38, no. 8, pp. 753–763, 2014.

25. Firouzian, A., M. D. Kelly, and J. M. Declerck, "Insight on automated lesion delineation methods for pet data," *EJNMMI research*, Vol. 4, no. 1, p. 69, 2014.

26. Zhuang, M., R. A. Dierckx, and H. Zaidi, "Generic and robust method for automatic segmentation of pet images using an active contour model," *Medical physics*, Vol. 43, no. 8, pp. 4483–4494, 2016.

27. Li, H., W. L. Thorstad, K. J. Biehl, R. Laforest, Y. Su, K. I. Shoghi, E. D. Donnelly, D. A. Low, and W. Lu, "A novel pet tumor delineation method based on adaptive region-growing and dual-front active contours," *Medical Physics*, Vol. 35, no. 8, pp. 3711–3721, 2008.

28. Chan, T. F., and L. A. Vese, "Active contours without edges," *IEEE Transactions on Image Processing*, Vol. 10, no. 2, pp. 266–277, 2001.

29. Abdoli, M., R. Dierckx, and H. Zaidi, "Contourlet-based active contour model for pet image segmentation," *Medical Physics*, Vol. 40, no. 8, 2013.

30. Jomaa, H., R. Mabrouk, and N. Khlifa, "Post-reconstruction-based partial volume correction methods: A comprehensive review," *Biomedical Signal Processing and Control*, Vol. 46, pp. 131–144, 2018.

31. Erlandsson, K., "Partial volume correction in pet imaging," in *Basic Science of PET Imaging*, pp. 355–378, Springer, 2017.

32. Bettinardi, V., I. Castiglioni, E. De Bernardi, and M. Gilardi, "Pet quantification: strategies for partial volume correction," *Clinical and Translational Imaging*, Vol. 2, no. 3, pp. 199–218, 2014.

33. Srinivas, S. M., T. Dhurairaj, S. Basu, G. Bural, S. Surti, and A. Alavi, "A recovery coefficient method for partial volume correction of pet images," *Annals of Nuclear Medicine*, Vol. 23, no. 4, pp. 341–348, 2009.

34. Sattarivand, M., M. Kusano, I. Poon, and C. Caldwell, "Symmetric geometric transfer matrix partial volume correction for pet imaging: principle, validation and robustness," *Physics in Medicine and Biology*, Vol. 57, no. 21, p. 7101, 2012.

35. Rizzo, G., I. Castiglioni, G. Russo, M. Tana, F. Dell'Acqua, M. Gilardi, F. Fazio, S. Cerutti, *et al.*, "Using deconvolution to improve pet spatial resolution in osem iterative reconstruction," *Methods of Information in Medicine*, Vol. 46, no. 2, pp. 231–235, 2007.

36. Teo, B.-K., Y. Seo, S. L. Bacharach, J. A. Carrasquillo, S. K. Libutti, H. Shukla, B. H. Hasegawa, R. A. Hawkins, and B. L. Franc, "Partial-volume correction in pet: validation of an iterative postreconstruction method with phantom and patient data," *Journal of Nuclear Medicine*, Vol. 48, no. 5, pp. 802–810, 2007.

37. Tohka, J., and A. Reilhac, "Deconvolution-based partial volume correction in raclopride-pet and monte carlo comparison to mr-based method," *Neuroimage*, Vol. 39, no. 4, pp. 1570–1584, 2008.

38. Kirov, A. S., J. Piao, and C. R. Schmidtlein, "Partial volume effect correction in pet using regularized iterative deconvolution with variance control based on local topology," *Physics in Medicine & Biology*, Vol. 53, no. 10, p. 2577, 2008.

39. Barbee, D. L., R. T. Flynn, J. E. Holden, R. J. Nickles, and R. Jeraj, "Partial volume correction of pet-imaged tumor heterogeneity using expectation maximization with a spatially varying point spread function," *Physics in Medicine and Biology*, Vol. 55, no. 1, p. 221, 2010.

40. Hoetjes, N. J., F. H. van Velden, O. S. Hoekstra, C. J. Hoekstra, N. C. Krak, A. A. Lammertsma, and R. Boellaard, "Partial volume correction strategies for quantitative fdg pet in oncology," *European Journal of Nuclear Medicine and Molecular Imaging*, Vol. 37, no. 9, pp. 1679–1687, 2010.

41. Hatt, M., A. Le Pogam, D. Visvikis, O. Pradier, and C. C. Le Rest, "Impact of partial-volume effect correction on the predictive and prognostic value of baseline 18f-fdg pet images in esophageal cancer," *Journal of Nuclear Medicine*, Vol. 53, no. 1, pp. 12–20, 2012.

42. Merlin, T., D. Visvikis, P. Fernandez, and F. Lamare, "A novel partial volume effects correction technique integrating deconvolution associated with denoising within an iterative pet image reconstruction," *Medical Physics*, Vol. 42, no. 2, pp. 804–819, 2015.

43. Sarder, P., and A. Nehorai, "Deconvolution methods for 3-d fluorescence microscopy images," *IEEE Signal Processing Magazine*, Vol. 23, no. 3, pp. 32–45, 2006.

44. Ayers, G., and J. C. Dainty, "Iterative blind deconvolution method and its applications," *Optics Letters*, Vol. 13, no. 7, pp. 547–549, 1988.

45. Fish, D., J. Walker, A. Brinicombe, and E. Pike, "Blind deconvolution by means of the richardson–lucy algorithm," *JOSA A*, Vol. 12, no. 1, pp. 58–65, 1995.

46. Guvenis, A., and A. Koc, "Optimising delineation accuracy of tumours in pet for radiotherapy planning using blind deconvolution," *Radiation Protection Dosimetry*, Vol. 165, no. 1-4, pp. 495–498, 2015.

47. Li, L., J. Wang, W. Lu, and S. Tan, "Simultaneous tumor segmentation, image restoration, and blur kernel estimation in pet using multiple regularizations," *Computer Vision and Image Understanding*, Vol. 155, pp. 173–194, 2017.

48. Koç, A., and A. Güvenış, "Implementation method in blind deconvolution based tumor segmentation using simulated pet images," in *Medical Technologies National Congress (TIPTEKNO), 2017*, pp. 1–4, IEEE, 2017.

49. Clark, K., B. Vendt, K. Smith, J. Freymann, J. Kirby, P. Koppel, S. Moore, S. Phillips, D. Maffitt, M. Pringle, *et al.*, "The cancer imaging archive (tcia): maintaining and operating a public information repository," *Journal of Digital Imaging*, Vol. 26, no. 6, pp. 1045–1057, 2013.

50. Muzi, Peter, Wanner, Michelle, Kinahan, and Paul, "The cancer imaging archive: Data from rider phantom pet-ct (2015)." `http://doi.org/10.7937/K9/TCIA.2015.8WG2KN4W`. Online; accessed 19 April 2016.

51. Tomei, S., A. Reilhac, D. Visvikis, N. Boussion, C. Odet, F. Giammarile, and C. Lartizien, "Oncopet_db: a freely distributed database of realistic simulated whole body 18f-fdg pet images for oncology," *IEEE Transactions on Nuclear Science*, Vol. 57, no. 1, pp. 246–255, 2010.

52. "Creatis.insa-lyon.fr (2017). softwares-releases creatis." `http://www.creatis.insa-lyon.fr/oncoPET_DB/`. Online; accessed 18 May 2015.

53. Papadimitroulas, P., G. Loudos, A. Le Maitre, M. Hatt, F. Tixier, N. Efthimiou, G. C. Nikiforidis, D. Visvikis, and G. C. Kagadis, "Investigation of realistic pet simulations incorporating tumor patient's specificity using anthropomorphic models: Creation of an oncology database," *Medical Physics*, Vol. 40, no. 11, 2013.

54. Beyer, T., D. W. Townsend, J. Czernin, and L. S. Freudenberg, "The future of hybrid imaging-part 2: Pet/ct," *Insights into Imaging*, Vol. 2, no. 3, pp. 225–234, 2011.

55. El-Gamal, F. E.-Z. A., M. Elmogy, and A. Atwan, "Current trends in medical image registration and fusion," *Egyptian Informatics Journal*, Vol. 17, no. 1, pp. 99–124, 2016.

56. Mahmoudzadeh, A. P., and N. H. Kashou, "Evaluation of interpolation effects on upsampling and accuracy of cost functions-based optimized automatic image registration," *Journal of Biomedical Imaging*, Vol. 2013, p. 16, 2013.

57. Jiang, S., P. Zhang, T. Han, W. Liu, and M. Liu, "Tri-linear interpolation-based cerebral white matter fiber imaging," *Neural Regeneration Research*, Vol. 8, no. 23, p. 2155, 2013.

58. McAuliffe, M. J., F. M. Lalonde, D. McGarry, W. Gandler, K. Csaky, and B. L. Trus, "Medical image processing, analysis and visualization in clinical research," in *Proceedings 14th IEEE Symposium on Computer-Based Medical Systems. CBMS 2001*, pp. 381–386, IEEE, 2001.

59. The MathWorks, I., "Image processing toolbox^{TM} user's guide version 9.2 (release 2015a)." `http://www.mathworks.com/`. Online; accessed 19 April 2015.

60. Conti, M., and M. E. Casey, "Estimating the optimal iteration number in iterative reconstruction: A statistical approach," in *Nuclear Science Symposium Conference Record, 2007. NSS'07. IEEE*, Vol. 6, pp. 4389–4394, IEEE, 2007.

61. Greffier, J., F. Macri, A. Larbi, A. Fernandez, E. Khasanova, F. Pereira, C. Mekkaoui, and J. Beregi, "Dose reduction with iterative reconstruction: optimization of ct protocols in clinical practice," *Diagnostic and Interventional Imaging*, Vol. 96, no. 5, pp. 477–486, 2015.

62. The National Institutes of Health Center for Information Technology (CIT), "Medical image processing, analysis and visualization (mipav) (version 7.3.0)." `http://mipav.cit.nih.gov/`, 2015.

63. Cabello, J., A. Bailey, I. Kitchen, M. Guy, and K. Wells, "Segmentation of low contrast-to-noise ratio images applied to functional imaging using adaptive region growing," in *Medical Imaging 2009: Image Processing*, Vol. 7259, p. 725940, International Society for Optics and Photonics, 2009.

64. Yushkevich, P. A., J. Piven, H. C. Hazlett, R. G. Smith, S. Ho, J. C. Gee, and G. Gerig, "User-guided 3d active contour segmentation of anatomical structures: significantly improved efficiency and reliability," *Neuroimage*, Vol. 31, no. 3, pp. 1116–1128, 2006.

65. Paul A. Yushkevich, G. G., "Itk-snap (version 3.6.0)." `http://itksnap.org`, 2017.

66. Kapur, J. N., P. K. Sahoo, and A. K. Wong, "A new method for gray-level picture thresholding using the entropy of the histogram," *Computer Vision, Graphics, and Image Processing*, Vol. 29, no. 3, pp. 273–285, 1985.

67. Caselles, V., R. Kimmel, and G. Sapiro, "Geodesic active contours," *International Journal of Computer Vision*, Vol. 22, no. 1, pp. 61–79, 1997.

68. Yushkevich, P. A., J. Piven, H. Cody Hazlett, R. Gimpel Smith, S. Ho, J. C. Gee, and G. Gerig, "User-guided 3D active contour segmentation of anatomical structures: Significantly improved efficiency and reliability," *Neuroimage*, Vol. 31, no. 3, pp. 1116–1128, 2006.

69. Zhou, H., G. Schaefer, and C. Shi, "Fuzzy c-means techniques for medical image segmentation," in *Fuzzy Systems in Bioinformatics and Computational Biology*, pp. 257–271, Springer, 2009.

70. IBM, C., "Ibm spss statistics for windows (version 23.0)." `http://www.ibm.com/analytics/us/en/technology/spss/`, 2015.

71. Laasmaa, M., M. Vendelin, and P. Peterson, "Application of regularized richardson–lucy algorithm for deconvolution of confocal microscopy images," *Journal of Microscopy*, Vol. 243, no. 2, pp. 124–140, 2011.

72. Xu, Z., M. Gao, G. Z. Papadakis, B. Luna, S. Jain, D. J. Mollura, and U. Bagci, "Joint solution for pet image segmentation, denoising, and partial volume correction," *Medical Image Analysis*, Vol. 46, pp. 229–243, 2018.